Human epidermis reconstructed from UV-B irradiated keratinocytes mimics epidermal ageing

INAUGURAL-DISSERTATION

to obtain the academic degree

Doctor rerum naturalium (Dr. rer. nat.)

submitted to the Department of Biology, Chemistry and Pharmacy

of Freie Universität Berlin

by

Lilian Julia Löwenau

from Berlin

2016

1st Reviewer: Prof. Dr. Monika Schäfer-Korting

Institute of Pharmacy (Pharmacology and Toxicology)

Freie Universität Berlin

Königin-Luise-Straße 2+4

14195 Berlin

2nd Reviewer: Prof. Dr. Gerhard Wolber

Institute of Pharmacy (Pharmaceutical and Medicinal Chemistry)

Freie Universität Berlin

Königin-Luise-Straße 2+4

14195 Berlin

Date of defense: 30. November 2016

This thesis was done under the supervision of

Prof. Dr. Monika Schäfer-Korting

Institute of Pharmacy (Pharmacology and Toxicology)

Freie Universität Berlin

Acknowledgements

First and foremost, I would like to express my gratefulness to **Prof. Dr. Monika Schäfer-Korting** for the opportunity to develop this PhD thesis as well as for her constant support and expert guidance.

I would like to thank **Prof. Dr. Gerhard Wolber** for the second opinion to this dissertation.

A PhD fellowship I gratefully received from the German Research Foundation (SFB 1112) and financial support from the project "Metabolic capacity of *in vitro* skin models" funded by the Federal Ministry of Education and Research (BMBF) enabled this work. I also thank the German Academic Exchange Service (DAAD) for financial support of the international conference meeting.

I would like to express my heartfelt gratitude to the entire working group of Pharmacology and Toxicology and to my fellow PhD students. I am deeply indebted to Prof. Dr. Günther Weindl for his scientific advice on this project and his supportiveness. I also want to extend my gratitude and thankfulness to Dr. Suvara Wattanapitayakul and to Hannelore Gonska. Specifically, I would like to thank Dr. Ruth Hirschberg and all PhD students and members of the SFB 1112.

Publication Record

Original Research Article

Lilian Julia Löwenau, Christian Zoschke, Robert Brodwolf, Pierre Volz, Christian Hausmann, Suvara Wattanapitayakul, Alexander Boreham, Ulrike Alexiev, Monika Schäfer-Korting: Increased Permeability of Reconstructed Human Epidermis from UV-stressed Keratinocytes. European Journal of Pharmaceutics and Biopharmaceutics (submitted)

Posters/Abstracts

Lilian J. Löwenau, S. Wattanapitayakul, J. M. Brandner, G. Weindl, and M. Schäfer-Korting: Human epidermis reconstructed from UVB-irradiated keratinocytes mimics premature ageing in human skin. 18th European Congress on Alternatives to Animal Testing (EUSAAT), Linz, Austria, 2013

Löwenau L, Weindl G, Schäfer-Korting M: A three-dimensional epidermis model reconstructed from UVB-irradiated keratinocytes mimics premature ageing in human skin. International Investigative Dermatology Meeting, Edinburgh, U.K., 2013

Zoschke C, **Löwenau LJ**, Wattanapitayakul S, Merk HF, Weindl G, Schäfer-Korting M (2014) Organotypic Models mimic Premature Ageing and Cutaneous Squamous Cell Carcinoma. 18. Jahrestagung der Gesellschaft für Dermopharmazie, Berlin, Germany, 2014

Löwenau L, Wattanapitayakul S, Brandner JM, Weindl G, Schäfer-Korting M: Human epidermis reconstructed from UVB-irradiated keratinocytes mimics premature ageing in human skin. 11th Meeting of the Epidermal Barrier Research Network (E^2BRN), Edinburgh, U.K., 2013

Monika Schäfer-Korting, Christian Zoschke, Stefan Hönzke, Ulrike Alexiev, Alexander Boreham, **Lilian Julia Löwenau**, Christian Hausmann, Leonie Wallmeyer, Julia Tigges, Jean Krutmann, Sarah Hedtrich, Ellen Fritsche: Reconstructed Human Skin Pioneers the Implementation of Diversity into Preclinical Testing in vitro. 20th European Congress on Alternatives to Animal Testing (EUSAAT), Linz, Austria, 2015

Awards and Scholarships

Scholarship SFB 1112 Nanocarriers: Architecture, Transport, and Topical Application of Drugs for Therapeutic Use, Freie Universität Berlin (03/2014-06/2015)

DAAD Travel Grant for the Investigative Dermatology Meeting, Edinburgh, U.K., 2013

Poster Award 18th European Congress on Alternatives to Animal Testing (EUSAAT), Linz, Austria, 2013

Poster Award Jahrestagung Gesellschaft für Dermopharmazie, Berlin, Germany, 2014

Table of Contents

1 Introduction

1. 1 Skin ageing

Aged skin is defined as skin of ≥ 50-year-old patients. It is characterized by decreased hydration (water loss), wrinkles, decreased pigmentation and higher susceptibility to irritants. Loss of elasticity is caused by degradation of collagens [1]. Most investigations to understand ageing processes in the skin refer to the dermis because of its collagen content, but recent studies have also focused on the age-related changes of the epidermis [2, 3]. In the epidermis, ageing processes include the symptoms of excessive dryness and pruritus [4]. Several years ago, a role for the epidermis in formation or deepening of wrinkles, that are commonly attributed to the dermis alone, has been described [5]. Other ageing effects include epidermal thinning (epidermal atrophy) and impaired wound healing. The changes of the barrier function that occur with aging possibly influence the permeability to drugs. Normal barrier function is sustained by keratinocytes undergoing proliferation, migration, differentiation and cornification in equilibrum [6]. Aged epidermis often consists of lower cell renewal rates, impaired differentiation [6] and increased desquamation by faster degradation of corneodesmosomes [3]. Age-related changes of the epidermis are relevant because the epidermis is the outermost barrier that protects the skin from the environment. Structural changes of the barrier influence its protective role.

1. 1. 1 Age-related changes of the epidermis

The protective function of the epidermis is largely defined by its potential for continuous renewal. Age-related epidermal thinning is a consequence of lower cell renewal rates [7]. Aged epidermis consists of less viable layers, where proliferation and differentiation of the keratinocytes is significantly reduced [6]. The proliferative potential of the aged epidermis is furthermore reduced by abundance of senescent cells that have zero proliferative potential [8]. Also, architectural changes of the extracellular matrix (ECM), with decreased lipid synthesis and lower secretion of lamellar bodies in the stratum corneum, lead to a porous ECM with less effective structural organization and compromised functions [9].

Aged epidermis is also changed in terms of calcium distribution [3]. Whereas in young epidermis, calcium concentrations are higher in the stratum granulosum than in all other layers, no such pattern is found in aged epidermis, where calcium levels are more homogenous. The calcium gradient is important for appropriate stratification, formation of the horny layer and barrier function. Therefore, the lack of this gradient in aged epidermis might lead to disturbed morphology.

In the epidermis, Langerhans cells in the viable layers present antigens to T-cells and activate the adaptive immune response. The epidermis is therefore also immunocompetent, which accentuates once more how important it is as a protective barrier against the environment. It protects the skin from invading microorganisms [10]. In the aged epidermis, fewer of these Langerhans cells are found and their functions are diminished [11]. The stratum corneum surface pH shifts with age; the acidic mantle becomes neutralized [12]. The pH shift reduces the population of beneficial bacteria on the surface which causes lower production of antimicrobial peptides (defensins) and further compromises the immunological function [3].

1. 2 Reconstructed skin

To test penetration and permeation of drugs in skin, a suitable test platform is needed. Although keratinocyte or fibroblast monolayers are useful to explain cell-specific effects, they lack skin-like features such as stratification and expression and location of differentiation markers. Excised human skin *ex vivo* poses the problem of fast degradation and storage effects. Non-human skin (mouse skin, pig skin) differs from human skin in regard to permeability and lipid composition, which limits its use. To overcome these drawbacks, reconstructed full-thickness skin and reconstructed epidermis has been developed [reviewed in van Gele, 2011[13]] and used to test phototoxicity, skin irritancy and permeation and penetration of various substances [14, 15].

In reconstructed epidermis, normal human keratinocytes are seeded onto suitable membranes. After formation of a keratinocyte monolayer, lifting of the constructs to the air-liquid interface initiates differentiation into a multilayered stratified epidermis [13]. Several commercial and in-house constructs of normal and diseased human full-thickness skin or

epidermis exist, but a skin model that mimics aged epidermis reconstructed from UV-pre-aged keratinocytes has not been established so far. Recent approaches to mimic aged skin involve premature induction of senescence in fibroblasts by mitomycin treatment [16], by prolonged cell culture periods [18] or the use of a glycated dermal compartment to mimic the age-related glycosylation observed in aged skin [17]. With the shortage of an appropriate model in mind, the study describes the attempt to mimic age-related changes of the epidermis in a novel type of RHE, where epidermal keratinocytes from juvenile skin were prematurely aged with the help of UV light.

1. 3 UV-induced cellular senescence

UV-B (280-320 nm) and UV-A (320-400 nm) light make for the most part of solar radiation reaching the earth surface, while UV-C (200-280 nm) is filtered by the ozone layer. As UV-B and UV-A are absorbed in the skin, with DNA as the strongest chromatophore, they have relevant biological effects. Excessive UV irradiation stress can lead to a DNA damage response followed by entry of severely damaged cells into apoptosis – or senescence [19]. Senescent cells are numerously found in aged tissues, which is why their abundance is considered a marker that indicates old age. A single dose of 25 mJ/cm^2 UV-B causes stress-induced senescence in keratinocytes independent of the donor age. This is why UV-B light was chosen here as the external stressor to induce senescence in an RHE.

1. 4 The role of cellular senescence in ageing

Ageing is a combination of intrinsic and extrinsic factors. Comparably little is known about the detailed mechanisms underlying ageing. The main theory is that senescent cells accumulate in tissues of the body and lead to the ageing phenotype so that the older the tissue, the more senescent cells [20]. Cellular senescence is a process that changes a cell so that it irreversibly loses the ability to divide. Cells undergoing senescence do not die, but are irreversibly arrested in the G1 phase of the cell cycle, yet remain in the tissue. Their metabolism is active (unlike cells undergoing apoptosis, necrosis, or quiescence). Cellular senescence is ascribed to the shortening of telomeres that occurs with every cell division. When a critical telomere length is reached, cells become unable to divide and senescent.

This is termed replicative or chronological senescence, as first described by Hayflick in 1965 [21]. Non-chronological, stress-induced senescence that occurs in response to DNA-damage by external stimuli (UV-B irradiation, for example) is independent of telomere status ("telomere-independent", "stress-induced" or "premature senescence") [22, 23].

1. 4. 1 Senescence as an anti-tumor mechanism

Cellular senescence is understood as a tumor suppressor mechanism. Cells that carry mutations must be hindered from replicating and becoming cancerogenic. It is thought that senescence is a way to retract cells that are too severely damaged to repair from the proliferative cell pool by mitotic arrest. Through secretion of pro-inflammatory cytokines, senescent cells gradually cause low-grade, chronic inflammation, alteration of tissue structure, and declined wound healing [24]. These deleterious effects are the "downside" of cellular senescence: senescence suppresses the development of cancer over the reproductive life span of an individual, but the accumulation of senescent cells contributes to impaired tissue function in later life [24, 25].

The development of certain age-related cancers (e. g. non-melanoma skin cancer, colon cancer) is supported by the pro-inflammatory and pro-tumorigenic environment of aged tissues, to which senescent cells and their secreted cytokines significantly contribute [24]. A theory of evolution can reconcile these seemingly contradictive findings: "Antagonistic pleiotropy" [26] claims biological processes are positively selected if they are beneficial during the reproductive life span (tumor suppression), however at the cost of deleterious effects in old individuals (pro-tumorigenic tissue environment, compromised tissue functions). Cellular senescence has been proposed to be an example of antagonistic pleiotropy.

Moreover, especially the UV-B content of solar radiation accounts for up to 90% of skin cancers, which mostly occur in later life. Excessive sun exposure in childhood was for a long time believed to be the only cause of the most frequent form of UV-related cancer, the non-melanoma skin cancer (NMSC). According to the theory, repeated, prolonged UV-B exposure

induces mutations in keratinocyte clones, which generate tumors in later life. This view is supported by the notion that 80% of all NMSC occur over the age of 60 [27]. Recently, the incomplete DNA damage response to UV that is observed in aged skin has been addressed: in this scenario, irreparably damaged keratinocytes are not efficiently removed. As a consequence, damaged cells that carry severe mutations still undergo mitosis and can form tumors [28, 29]. It is possible that this inaccurate DNA damage response contributes to the prevalence of skin cancers in older individuals.

1. 4. 2 Characteristics of senescent cells

Senescent cells are characterized by an increased and flattened cell surface. Their outstretched appearance is caused by the formation of actin-stress-fibers with focal adhesion contacts where accumulation of vinculin can be found. The flattening of senescent cells is associated with their lack of migratory properties [30, 31], which contributes to the poor wound healing in old patients. Senescent cells also have prominent Golgi apparatuses and strong vacuolization of the cytoplasm, together with increased granulation [32]. Accumulations of damaged but incompletely degraded proteins, mitochondria and lipids are found in the cytoplasm. This is due to the decreased function of the lysosomes in senescent cells that provide degradation and recycling of non-functional proteins and other elements in normal cells [32].

Senescent cells also display nuclear modifications. They involve the size of nuclei in relation to the cytoplasm [33], the shape of the nuclear lamina, the nucleoli as well as the total number of nuclei per cell [32]. Multinucleation might even be a consequence of the incomplete cellular recycling processes typical of senescent cells, including insufficient breakdown of the nuclear envelope. Irresponsiveness to proliferative stimuli and resistance to apoptosis [34] are also considered hallmark features of senescence. Other features associated with senescence include senescence-associated heterochromatin foci (SAHF), characterized by dense chromatin structures. SAHF formation is mediated via a DNA-damage response signal that activates histone modification γH2AX [35]. It is discussed whether the chromatin remodeling has a functional role in senescence, suggesting that it suppresses the

transcription of genes involved in cell cycle progression, as senescent cells are resistant to proliferative stimuli (reviewed in [40]).

1. 4. 3 Senescence-associated secretome (SASP)

Senescent cells secrete a special set of cytokines and growth factors called the SASP (Senescence-associated secretory phenotype or -secretome)[24]. These include elevated levels (compared to normal, proliferative cells) of IL-1α, IL-1ß, IL-6, -7, -8, 13, TNFα, HGFs, VEGFs, MMPs (Matrix-metalloproteinases) and GM-CSF (granulocyte macrophage colony-stimulating factor). The secretome is highly conserved between mice and humans. As most of the proteins of the SASP are pro-inflammatory, they explain the chronic low-level inflammation in aged tissues. Since chronic inflammation ultimately contributes to the development of cancer, this is in accordance with the observation that most cancers occur later in life [24, 27]. The SASP is regarded as the main cause for the deleterious effects of senescence, since several of its components can disrupt tissue structure and function and promote cancer progression [24]. Several mechanisms are discussed on how maintenance of the SASP is regulated during senescence. Contrarily to other senescent features (proliferative arrest, SAHF formation), the SASP is not regulated by p53. Instead, the role of p38 MAP kinase on IL-1α/NFkB signaling as well as the mTOR pathway are discussed [37].

1. 4. 4 Transcription factor (p53)-mediated senescence

UV-light, reactive oxygen species (ROS) and other potential mutagens are constantly threatening the integrity of the genome. The induction of cell cycle arrest is a DNA damage response that allows for DNA repair. A repair complex is built that induces transcription factor p53, a critical regulator of cell survival in stress signaling. p53 is a tumor suppressor protein that regulates apoptosis in response to DNA damage and plays a key role in both replicative and stress-induced senescence through UV-B exposure [38, 39]. If DNA damage turns out to be irreparable, p53 mediates entry into apoptosis - or senescence. It was shown previously that p53 and its downstream effector $p21^{WAF1}$ are important for entry into senescence. $p21^{WAF1}$ together with $p16^{INK4a}$ in a concerted function maintain the suppression of proliferation during senescence. Namely $p16^{INK4a}$ is a negative cell cycle regulator that

inhibits the cyclin-dependent kinase cyclin D so that suppression of proliferation remains active and therefore arrests the cell cycle at the G1 phase. $P16^{INK4a}$ induces premature senescence but is also overexpressed in chronologically aged tissues. $P21^{WAF1}$ is less specific and able to inhibit cell cycle progression at many stages (reviewed in [40]).

Yet, neither activated $p16^{INK4a}$ nor p21 are indispensable for senescence; inhibition of $p16^{INK4a}$ still allows growth arrest. Redundant mechanisms may exist that are able to induce senescence despite lack of $p16^{INK4a}$ (for a review see [40]). Also in the case of p53, conflicting data on its role in senescence has been reported [41]. A concerted function of p53, $p21^{WAF1}$ and $p16^{INK4a}$ on cell cycle arrest necessary for senescence has been proposed: up- or down-regulation of proliferation-inhibitory as well as proliferation-stimulating genes has been observed in senescent cells, but also less specifically in some terminally differentiated cells. This lack of a distinct senescence-specific regulation pattern makes it difficult to detect senescent cells by their gene expression [38].

1. 4. 5 Detection of senescent cells

The most widely used and reliable marker for the detection of senescent cells is the expression of lysosomal SA- (Senescence-associated) ß-galactosidase [42, 43]. Senescent cells have enlarged lysosomes and display increased activity of ß-galactosidase compared to normal, proliferative cells. In the cell, ß-galactosidase conveys the hydrolysis of ß-galactosides into monosaccharides. While ß-galactosidase operates at pH 3-4 in normal cells, senescent cells display additional ß-galactosidase activity at pH 6 [44]. This additional activity is detected via a colorimetric assay, where the substrate X-Gal [42, 45] is cleaved into a blue-greenish precipitate. The maintenance of pH 6 is essential for the assay. The increased activity at suboptimal pH also correlates with a total increase of ß-galactosidase protein levels [44]. Yet, the function of this additional expression for the senescent state has not been elucidated. Although ß-galactosidase overexpression does not seem functionally required for senescence, it has remained the preferred biomarker for detection of senescent cells.

1. 5 UV-B irradiation dose evaluation

In this study, keratinocytes were stressed with UV-B light **before** seeding into inserts. In most experiments addressing UV-B effects, the skin (or skin construct) is irradiated after maturation of the barrier function. For example, increased apoptosis and DNA-damage markers were observed in a commercially purchased epidermis equivalent, which was then exposed to 100 mJ/cm^2 UV-B [46]. Treated with 10-40 mJ/cm^2, other epidermis equivalents displayed differential expression and activity of hyaluronidase [47] and functional deterioration of tight-junction proteins [48], which are crucial for intact barrier function [49]. Because they lack the UV-absorbing barrier of intact skin, UV-B doses administered directly to cultured keratinocytes (this study) cannot be compared to UV-B doses administered to RHE or RHS with functional barrier (or to excised human skin *ex vivo*). Therefore, UV-B doses from the literature that had been applied to monolayer keratinocytes were regarded as suitable for the UV irradiation of keratinocytes and reconstruction of UV-RHE in this study.

1. 5. 1 UV B-dependent cell viability and proliferation

To assess the effect of different UV doses, keratinocyte monolayers were not only tested for senescent cells to appear but also for effects on viability and proliferation. Previous studies report that irradiation with 40 mJ/cm^2 UV-B reduced the viability of HaCaT keratinocytes by 50% after 24 h, and up to 100% at doses greater than 40 mJ/cm^2 [50]. 20 and 33 mJ/cm^2 UV-B had no effect, while 67 mJ/cm^2 UV-B reduced the viability by almost 100% after 24h [51]. These results are supported by another study that found 20-40 mJ/cm^2 UV-B had no effect on the viability in neither HaCaT nor primary keratinocytes, while higher doses (60, 80 mJ/cm^2) caused a significant decrease [52]. UV-B induced mortality is caused by both necrosis (indicated by release of lactate dehydrogenase) and apoptosis (indicated by caspase activity and DNA fragmentation) [19].

Regarding the effect on proliferation, irradiation of primary keratinocytes with 12.5 and 25 mJ/cm^2 UV-B reduced the proliferation by 30% after 10 days [19]. There is much controversy as to whether UV irradiation increases or decreases proliferation in keratinocytes; supposedly the effects depend largely on the applied doses. In the literature, the UV-B doses

defined as mortal and anti-proliferative vary greatly, which is explained by the use of an array of different devices and light bulbs from different manufacturers for the emission of UV light. Most studies are devoid of an actual verification of the administered doses. Unfortunately, direct comparisons are rather difficult.

1. 6 Percutaneous uptake and skin barrier function

In aged skin, decreased cohesiveness and altered lipids of the stratum corneum [9, 53] change the properties of the barrier function. The intercellular lipid domains of the stratum corneum are the main route for the majority of small molecules and drugs permeating the human epidermis. Investigating the barrier function in terms of both permeation and penetration of small and larger molecules would be particularly interesting in an RHE that mimics aged epidermis.

1. 6. 1 Penetration and permeation

Considering the sufficient uptake of cosmetics and drugs into skin, the stratum corneum brings about the main challenge to overcome. It is rather impermeable for substances with a molecular weight above 500 Da [54]. Conventional drug formulations in the form of creams and ointments only allow for 1-2 % uptake of the administered drug. This generally leaves about large quantities of non-penetrated remains, which is why efficient carrier systems are needed [55]. Critical for the risk assessment of different types of carriers is their application on diseased, barrier-impaired skin, which also includes aged skin that often has a decreased barrier function. In this regard, the testing of drug carrier penetration on reconstructed epidermis from UV-stressed keratinocytes is particularly interesting.

Also, to test the predictive power of this novel type of RHE according to the procedures of the validation study for reconstructed epidermis [98], two OECD reference compounds were used. Their permeation coefficients can indicate in how far the normal and UV-RHE pass as appropriate test platforms for permeation testing.

1. 6. 1. 1 Nanoparticle-enhanced penetration

In order to improve the penetration/permeation of human skin, nanoparticles as drug carriers for the treatment of skin diseases have moved to the focus of attention [55, 56]. To which extent nanocarriers are able to overcome the stratum corneum and penetrate into the viable skin layers is subject to discussion. The consensus as summarized by the Scientific Committee on Consumer Products (SCCP) in 2007 was that nanoparticles with sizes smaller than 10 nm penetrate, at least to some extent, into viable layers of healthy skin while nanoparticles greater than 20 nm fail to penetrate therein. The renal cut-off value limits the excretion of macromolecules, which is why it s so important to assess the possible risk of nanocarriers to enter the vascular system [57]. This especially becomes a concern in the treatment of aged skin, where epidermal atrophy, impaired differentiation and increased desquamation influence the barrier function [3, 6]. An RHE that mimics age-related changes would be very useful for the risk assessment of nanocarriers.

The efficacy of lipid-based nanoparticles for drug delivery to the skin has been outmatched by yet another type of dendritic nanocarriers, the core-multishell (CMS) nanocarriers [58]. It has been shown that CMS nanocarriers clearly enhance penetration of the lipophilic model dye Nile red into excised human skin and skin constructs [59]. Also for more hydrophilic substances and a hydrophilic model dye, penetration enhancement could be observed [60]. Küchler et al. showed two-fold increased penetration of the hydrophilic dye rhodamin B compared to penetration in a base cream [61]. CMS nanocarriers consist of a polyglycerole core surrounded by a hydrophilic outer- and lipophilic inner shell. Their total size is 3-5 nm in diameter; still they can form larger aggregates [60]. Nile red is released from the shell of the carrier at skin surface temperature (32°C) [62]. The location of the CMS nanocarriers themselves can be tracked in the tissue via indocarbocyanine labeling. The indocarbocyanine (ICC) is covalently bound to the inner shell.

The penetration of Nile red loaded onto CMS nanocarriers as well as the penetration of CMS nanocarriers themselves has been studied for different skin models [63]. Among those were knock-down models of different keratinization disorders [59] as well as hyperkeratotic peeling skin disease and non-melanoma skin cancer [64, 65]. The results showed that

penetration of Nile red as well as of the carriers themselves increased significantly with perturbance of the barrier function [64]. The disease models displayed different thickness, lipid composition and functional differences of the stratum corneum. This layer has the largest influence on the penetration of nanocarriers. CMS nanotransporters have been tested on different skin models but not yet been tested on an RHE to mimic aged skin.

1. 7 Aim and outline of the thesis

Several commercial and in-house constructs of reconstructed normal and diseased human full-thickness skin (RHS) or epidermis (RHE) exist. Attempts have been made to generate skin models that mimic the properties of aged skin. Among these are full-thickness skin equivalents that use a glycated dermal compartment to mimic the influence of age-related glycation in skin [17], or fibroblasts induced to premature senescence by mitomycin treatment [16]. Here, it was intended to mimic aged epidermis by an RHE constructed from UV-irradiated keratinocytes. The UV-RHE was investigated in different aspects (morphology, secretome, gene expression, senescence markers) that are characteristic of aged skin *in vivo* and used to test percutaneous absorption of OECD reference compounds and core-multishell nanocarriers.

2 Material

2. 1 Technical devices and consumptive materials

Autoclave – Systec, Wettenberg, Germany

Balances – Sartorius, Göttingen, Germany

Beta-Counter 1450 Microbeta Plus LSC – Perkin Elmer, Rodgau, Germany

Cell counter (0.0025 mm^2/0.1 mm), Neubauer improved – Carl Roth, Karlsruhe, Germany

Cell culture flasks, TPP Tissue Cell Culture (75 cm^2) – TPP, Trasadingen, Switzerland

Cell Culture Inserts, 0.4 µm PCF, 12 mm Diameter – Merck Millipore, Darmstadt, Germany

Centrifuge Eppendorf 5415D – Eppendorf, Hamburg, Germany

Centrifuge Megafuge 1.0 R – Heraeus, Hamburg, Germany

Centrifuge Heraeus Pico 17 – Heraeus, Hamburg, Germany

Cover slips 24 x 50 mm – Carl Roth, Karlsruhe, Germany

Digital microscope, BZ-8000 – Keyence, Neu-Isenburg, Germany

Electrophoresis chamber – Bio-rad, München, Germany

Easypet© – Eppendorf, Hamburg, Germany

Filtration system Millipore®– Merck Millipore, Darmstadt, Germany

Filtropur S 0.2 µm – Sarstedt, Nümbrecht, Germany

FluoStar Optima – BMG Labtech, Offenburg, Germany

Incubator Heracell 240i – Thermo Fisher Scientific, Waltham, USA

Incubator Heraeus Function Line Typ B6 – Thermo Fisher Scientific, Waltham, USA

LaminAir Sterile working bench HB2472 – Heraeus, Hanau, Germany

LightCycler® 480 Instrument – Roche, Mannheim, Germany

LightCycler® 480 Software – Roche, Mannheim, Germany

Magnetic plate stirrer RO 10 power IKAMAG – IKA Werke GmbH, Staufen, Germany

Microscopy slides Polylysine – Thermo Fisher Scientific, Waltham, USA

Microtome Leica CM 1510-S1 – Leica, Bensheim, Germany

Parafilm sealing foil – Bemis Healthcare Packaging, Londonderry, UK

Neutral density filter (grey filter) OD 0.5 – Physics department (Freie Universität)

Phase Contrast Inverted Microscope, Axiovert 135 – Carl Zeiss, Jena, Germany

Pasteur pipettes – Carl Roth, Karlsruhe, Germany

Petri dishes, 87 mm diameter – TPP, Trasadingen, Switzerland

Pipette Research© – Eppendorf, Hamburg, Germany

Pipette TPP serological – TPP, Trasadingen, Switzerland

Pipette tips – Sarstedt, Nürnbrecht, Germany

Plates (6-well) – TPP, Trasadingen, Switzerland

Plates (96-well for ELISA) – Sigma-Aldrich, München, Germany

Plates (96-well for BCA Assay) – Thermo Fisher Scientific, Waltham, USA

Plates (96-well for PCR) – BioOne, Frickenhausen, Germany

PVDF membrane Immobilon P – Merck Millipore, Darmstadt, Germany

Scalpel – Swann-Morton, Sheffield, UK

Scalpel blades – Swann-Morton, Sheffield, UK

Scintillation cocktail Optiphase Supermix – Perkin Elmer, Rodgau, Germany

Sealing Foil for 96-well plate (PCR) – BioOne, Frickenhausen, Germany

Stainless steel beads, 5 mm diameter – Qiagen, Hilden, Germany

Syringes – Sarstedt, Nümbrecht, Germany

Tissue Lyser II – Qiagen, Hilden, Germany

Tubes, Cell culture (15, 50 ml) – TPP, Trasadingen, Switzerland

Tubes, Eppendorf safe-lock (1.5, 2 ml) – Eppendorf, Hamburg, Germany

Tubes, PCR nuclease-free (0.5 ml) – Carl Roth, Karlsruhe, Germany

Ultrasonic bath Sonorex RK 100 – Bandelin, Berlin, Germany

UV irradiation chamber – Vilber-Lourmat, Eberhardzell, Germany

UV-B light bulbs (mercury-vapor lamps) – Vilber-Lourmat, Eberhardzell, Germany

Vortexer Vortex Genie 2 – Scientific Industries Inc., New York, USA

2. 2 Reagents

1, 2, 6, 7-^{3}H-Testosterone (100 Ci/mmol) – Amersham, Freiburg, Germany

1-Methyl-^{14}C-caffeine (51.2 Ci/mmol) – Perkin Elmer, Rodgau, Germany

Ammonium persulfate – Carl Roth, Karlsruhe, Germany

ß-galactosidase Senescent Cells Staining Kit – Sigma-Aldrich, München, Germany

Bromophenol blue – Carl Roth, Karlsruhe, Germany

CellnTec culture media – CellnTec, Bern, Switzerland

Cell Proliferation kit ELISA (colorimetric) – Roche, Mannheim, Germany

DAPI Antifading mounting medium – Dianova, Hamburg, Germany

Dispase II – Roche, Mannheim, Germany

DMEM (Dulbecco's Modified Eagle's Medium) – Sigma-Aldrich, München, Germany

DMSO (dimethyl sulfoxide) – Sigma-Aldrich, München, Germany

ECL Reagent SignalFire – New England Biolabs, Frankfurt, Germany

EDTA (ethylene diamine tetraacetic acid) – Sigma-Aldrich, München, Germany

ELISA Kit IL-1α, IL-6, -8, -12, TNFα – R&D Systems, Wiesbaden, Germany

Eosin Y – Carl Roth, Karlsruhe, Germany

Glycin – Sigma-Aldrich, München, Germany

Goat serum – Dianova, Hamburg, Germany

Hematoxylin solution according to Meyer – Carl Roth, Karlsruhe, Germany

Hydrogen peroxide 30 % – Carl Roth, Karlsruhe, Germany

Igepal-630 – Carl Roth, Karlsruhe, Germany

KBM (Keratinocyte basal medium) – Lonza, Walkersville, USA

L-Glutamine – Biochrome, Berlin, Germany

MTT – Sigma-Aldrich, München, Germany

Nonfat Dry Milk Powder Sucofin – TSI GmbH & Co. KG, Zeven, Germany

Primary antibody: Polyclonal ab to Galactosidase Beta – Cloud-Clone Corp., Houston, USA

Primary antibody: Monoclonal ab to beta-actin – Cell Signaling Technology, Cambridge, UK

Primary antibody: Monoclonal ab to Vinculin – Abcam, Cambridge, UK

Primary antibody: Monoclonal ab to γH2AX – Abcam, Cambridge, UK

Primary antibody: Monoclonal ab to $p16^{INK4a}$ – Abcam, Cambridge, UK

Primary antibody: Monoclonal ab to Keratin 10 – Dianova, Hamburg, Germany

Primary antibody: Monoclonal ab to Keratin 14 – Dianova, Hamburg, Germany

Primary antibody: Monoclonal ab to Involucrin – Dianova, Hamburg, Germany

Primary antibody: Monoclonal ab to Fillaggrin – Dianova, Hamburg, Germany

Primary antibody: Monoclonal ab to Claudin-1 – Dianova, Hamburg, Germany

Protease/Phosphatase Inhibitor Cocktail – New England Biolabs, Frankfurt, Germany

Protein Assay Kit Pierce BCA Protein Assay – Thermo Fisher Scientific, Waltham, USA

Protein marker Western-C Precision Protein – Bio-rad, München, Germany

Protein marker (biotynylated), HRP-conjugated – Bio-rad, München, Germany

RNA isolation NucleoSpin RNA II kit – Macherey-Nagel, Düren, Germany

RotiHistofix® – Carl Roth, Karlsruhe, Germany

RotiHistol® – Carl Roth, Karlsruhe, Germany

RotiHistokitt® – Carl Roth, Karlsruhe, Germany

Rotiphorese® Gel 40 (37.5:1) – Carl Roth, Karlsruhe, Germany

Rotiphorese® Gel 40 (29:1) – Carl Roth, Karlsruhe, Germany

SDS (sodium dodecyl sulfate) – Sigma-Aldrich, München, Germany

Secondary antibody: anti-biotin HRP-conjugated ab – Bio-rad, München, Germany

Secondary antibody: anti-ß-actin ab – Cell Signaling Technology, Cambridge, UK

Secondary antibody (IF): α-mouse ab DyLight 594 – Dianova, Hamburg, Germany

SYBR Green Master I – Roche, Mannheim, Germany

TEMED – Carl Roth, Karlsruhe, Germany

TMB (tetramethyl benzidine) – Sigma-Aldrich, München, Germany

Tissue freezing medium – Leica, Nussloch, Germany

TRIS – Carl Roth, Karlsruhe, Germany

Trypsine – Biochrome, Berlin, Germany

Tween 20 – Carl Roth, Karlsruhe, Germany

2. 3 Culture media and solutions:

	Transport medium
DMEM supplemented with:	Penicillin 100 I.U./ml
	Streptomycin 100 µg/ml

	KGM
KBM supplemented with:	BPE
	Insulin
	hEGF
	Hydrocortisone
	Gentamicin
	Amphotericin B

	Stop medium
DMEM supplemented with:	10 % FCS
	100 I.U./ml penicillin
	100 µg/ml streptomycin

	KC differentiation medium CnT-02-3DP
	Reagent A (not specified by the company)
CnT-57-S supplemented with:	
	Reagent B (not specified by the company)
	Reagent C (not specified by the company)

All CellnTec culture media were free from antibiotics and antimycotics.

	PBS
ddH_20 supplemented with:	0.2 g/l KCl
adjusted to pH 7.4	8 g/l NaCl
	0.2 g/l KH_2PO_4
	1.44 g/l Na_2HPO_4

	Trypsin-EDTA
PBS supplemented with:	1.67 mg/ml Trypsin
	0.67 mg/ml EDTA

2. 4 Solutions for ELISA:

	Wash buffer
PBS supplemented with:	0.05% Tween 20

	Reagent diluent
IL-8:	0.1% BSA 0.05% Tween 20 in TBS (20 mM Trizma base, 150 mM NaCl)
IL-1α, -6, -12p70, TNFα:	1% BSA in PBS pH 7.2-7.4; 0.2 µm filtered

	Block buffer
PBS supplemented with:	
IL-8:	1% BSA 0.05% NaN_3
IL-1α, -6, -12p70, TNFα:	1% BSA in PBS pH 7.2-7.4; 0.2 µm filtered

Substrate solution
11 ml Citrate buffer 110 µl TMB solution 3.3 µl H_2O_2, 30%

Citrate buffer
40 mM citric acid solution 0.2 µm filtered adjusted to pH 3.95

TMB solution
2% Tetramethylbenzidine in DMSO/Ethanol (1:1) 0.2 µm filtered

ELISA stop solution
1N HCl (conc. HCl, 37% = 12.11 mol/l)

2. 5 Solutions for cDNA synthesis and RT-qPCR:

cDNA synthesis:

1 µl random hexamer primer (0.2 µg/µl)
4 µl 5x reaction buffer
1 µl RiboLock ribonuclease inhibitor (20 u/µl)
2 µl 10 mM dNTP mix
1 µl RevertAid M-MuLV reverse transcriptase (200 u/µl)

Solutions for RT-qPCR:

DEPC-treated water

ad 1 l ddH_2O: 1 ml DEPC
stored at RT for 24°C, then autoclaved

70% Ethanol

772.7 µl/ml Ethanol 96 %
227.3 µl/ml DEPC-treated water

Lysis Buffer

3.5 µl ß-mercaptoethanol
227.3 µl/ml DEPC-treated water

PCR Mastermix:

0.5 µl forward primer
0.5 µl reverse primer
2 µl DNA template
5 µl SYBR® Green

Target gene	Forward primer sequence	Reverse primer sequence
cyclin D2	5'-TACTTCAAGTGCGTGCAGAAGGAC-3'	5'-TCCCACACTTCCAGTTGCGATCAT-3'
p16	5'-TTATTAGAGGGTGGGGCGGATCGC-3'	5'-GACCCCGAACCGCGACCGTAA-3'
vegf-c	5'-CCATGCAGATCATGCGGATCA-3'	5'-CCTTGGCTTGTCACATCTGCAA-3'
p53	5'-GCCCAACAACACCAGCTCCT-3'	5'-CCTGGGCATCCTTGAGTTCC-3'
mmp-1	5'GAGATCATCGGGACAACTCTCCTT-3'	5'GTTGGTCCACCTTTCATCTTCATCA-3'
nfkb	5'-TAAGCAGAAGCATTAACTTCTCTGGA-3'	5'-CCTGCTTCTGTCTCTAGGAGAGTA-3'
gapdh	5'-GAGTCAACGGATTTGGTCGT-3'	5'-GACAAGCTTCCCGTTCTCAG-3'

2. 6 Solutions for detection of ß-galactosidase

Western Blotting

Protein quantification (BCA Protein quantification kit contents):

BCA Reagent A	
in 0.1 M sodium hydroxide:	sodium carbonate sodium bicarbonate bicinchoninic acid sodium tartrate concentrations not specified by the company

BCA Reagent B
(containing 4% cupric sulfate)

Albumin Standard
2.0 mg/ml BSA in 0.9% saline 0.05% sodium azide

Gel electrophoresis and blotting:

SDS running gel
3 ml Rotiphorese® Gel 40 (37.5:1) 2.4 ml Running gel buffer 1.2 ml SDS 1% 5.4 ml ddH_2O 10 µl TEMED 60 µl APS 10%

SDS stacking gel
0.5 ml Rotiphorese® Gel 40 (37.5:1) 0.8 ml Stacking gel buffer 0.4 ml SDS 1% 2.3 ml ddH_2O 4 µl TEMED 20 µl APS 10%

Running buffer

50 ml 10x buffer
450 ml ddH_2O

Blotting buffer

110 ml 10x transfer buffer
990 ml ddH_2O

TBS 10x

12.144 g Tris HCl (100 mM)
87.66 g NaCl

TBST

100 ml TBS (10x)
900 ml ddH_2O
1 ml Tween 20

Block buffer

5% (w/v) non-fat dry milk
in TBST

Primary antibodies

Polyclonal ab to ß-galactosidase 1: 250
Monoclonal ab to ß-actin 1: 1000

Secondary antibodies

anti-biotin HRP-conjugated 1: 5000
anti-ß-actin 1: 1000

Colorimetric pH-dependent assay of SA-ß-galactosidase:

Fixation buffer 10x

20% formaldehyde
2% glutaraldehyde
70.4 mM Na_2HPO_4
14.7 mM KH_2PO_4
1.37 M NaCl
26.8 mM KCl

ß-galactosidase staining

For one 6-well-plate (10 ml):	1 ml of Staining Solution 10×(not specified)
	125 µl of Reagent B (400 mM Potassium Ferricyanide)
	125 µl of Reagent C (400 mM Potassium Ferrocyanide)
	0.25 ml of X-gal Solution (40 mg/ml; not specified)
	8.50 ml of 0.2 filtered ddH_2O

2. 7 Solutions for BrdU-Incorporation Assay:

BrdU labeling reagent

1000x 10 mM 5-bromo-2'-deoxyuridine in PBS pH 7.4

Fixation buffer

FixDenat (not specified by the company)

Anti-BrdU-POD

peroxidase-conjugated monoclonal antibody from mouse-mouse hybrid cells, clone BMG 6H8, fab fragments
Antibody dilution solution: not specified by the company

Substrate solution

Tetramethyl-benzidine (concentration not specified)

2. 8 Solutions for Immunofluorescence:

Wash buffer

PBS supplemented with:	0.0025% BSA
	0.025 % Tween 20

Blocking solution

PBS supplemented with:	5 % goat serum

Primary antibodies	
diluted in PBS 0.0025% BSA, 0.025 % Tween 20:	mouse monoclonal ab to Vinculin 1:100
	mouse monoclonal ab to γH2AX 1:250
	mouse monoclonal ab to $p16^{INK4a}$ 1:50
	mouse monoclonal ab to Cytokeratin 10 1:200
	mouse monoclonal ab to Cytokeratin 14 1:200
	mouse monoclonal ab to Involucrin 1:100
	mouse monoclonal ab to Fillaggrin 1:200
	mouse monoclonal ab to Claudin-1 1:100

Secondary antibodies	
diluted in PBS 0.0025% BSA, 0.025 % Tween 20:	α-mouse ab DyLight 594 1:400
	α-rabbit ab DyLight 488 1:400

2. 9 Solutions for Permeation experiments:

Stock solution caffeine
1 mg/ml caffeine
in PBS

Radioactively labeled ^{14}C caffeine
1.85 MBq
in 500 µl EtOH
0.0499 mCi

The stock solution was spiked with radioactively labeled caffeine to 2 µCi/ml (0.074 MBq/ml). 20 µl ^{14}C-caffeine was added per 1 ml caffeine stock solution. For the permeation experiment, 1.5 mg caffeine was solved in 1.5 ml PBS. 30 µl ^{14}C-caffeine was added. Of this donor solution with an activity of 2 µCi/ml (0.074 MBq/ml), 150 µl per reconstructed epidermis was applied. Infinite-dose approach conditions were maintained (387.4 µg/cm^2 caffeine). Calibration caffeine: standard 1 = 10 µl donor solution + 990 µl PBS (0.01 mg/ml); standard 2 = 100 µl s 1 + 900 µl PBS (0.001 mg/ml).

Stock solution testosterone

40 µg/ml testosterone
in PBS Igepal (50:1)

Radioactively labeled 1,2,6,7-^{3}H-testosterone

37 MBq
in 1 ml
1 mCi

For the permeation experiment, 15 mg testosterone was added to 1.5 ml ethanol absolut. Of this testosterone stock solution, 60 µl was added to PBS with igepal as solubilizer to a total volume of 15 ml. The stock solution was then spiked with radioactively labeled testosterone. 2 µl 1,2,6,7-^{3}H-testosterone was added to 1 ml testosterone stock solution. Of this donor solution with an activity of 2 µCi/ml (0.074 MBq/ml), 150 µl per insert was applied. Infinite-dose approach conditions were maintained (15.4 µg/cm^{2} testosterone). Calibration testosterone: standard 1 = 100 µl donor solution + 900 µl PBS (0.004 mg/ml); standard 2 = 100 µl s 1 + 900 µl PBS (0.0004 mg/ml).

3 Methods

3. 1 Cultivation and UV-B irradiation of human keratinocytes

Keratinocytes isolated from juvenile foreskin were cultivated at 37°C with 5% CO_2 until reaching 80% confluency. The cells were collected by trypsinization. The reaction was stopped with DMEM + 5% calf serum. After centrifugation at 10.000 rpm and RT for 5 min, keratinocytes were resuspended in KGM. They were adjusted to a density of 3 x 10^5 cells/ml. For each irradiation dose and the mock-irradiation (control), 1 ml of the suspension containing 300.000 cells was placed into a 6-well plate. The plate was exposed to UVB at 9.6 (25, 30) mJ/cm^2. The plate with mock-irradiated keratinocytes was put into the UV-B irradiation chamber without starting the program. The UVB source delivered the peak spectrum at 312 nm and energy at the rate of 4.28 mJ/second.

3. 1. 2 Determination of UV-B irradiation

To obtain a UV-B dose of 9.6 mJ/cm^2, a programmed dose of 30 mJ/cm^2 was applied together with a neutral density filter (grey filter) of OD 0.5 (kindly provided by Prof. Dr. Ulrike Alexiev, Freie Universität Berlin, Physics Department):

Optical density (d) of the filter
Applied intensity (I_0)
Measurable intensity (I) after the filter, calculates according to the Physics department as:

$I / I_0 = 10^{-d}$
$I = 10^{-0.5}$ x 30 mJ/cm^2
$I = 9.6$ mJ/cm^2

3. 2 Keratinocyte monolayers

For **cell viability** assays 24 (48) h post-irradiation, cells were incubated with 100 µl (5 mg/ml) MTT solution in 1 ml KGM per well for 4 h followed by complete removal of the MTT and KGM and addition of 1 ml DMSO per well. The plates were briefly vortexed to allow complete dissolving of the crystals. Absorption was measured at 540 nm. DMSO was used as blank. Viability of the cells in response to UV-B irradiation was calculated. The mock-treated control was assigned as 100% viability. An additional sample had 10% DMSO added to the cells (cytotoxic) and was used as the positive control.

For **cell proliferation** assays 48 (72) h post-irradiation, Roche Cell Proliferation Kit ELISA (colorimetric) was used. Cells were incubated with 100 µl labeling solution of the pyrimidine analogue BrdU added directly to the cultured cells to a concentration of 10 µM BrdU per well and incubated for 8 h at 37°C. After removing the labeling solution, the cells were fixed for 30 min at RT with 1 ml FixDenat fixing solution. After removal of the fixing solution, the cells were incubated with 1 ml anti-BrdU POD working solution for 2 h at RT. After washing (1 ml PBS per well, 3x), cells were incubated with 1 ml tetramethyl-benzidine for 5 min at RT. After 5 min, 250 µl 1 N HCl were added to stop the reaction and the absorption was measured at 450 nm. The percentage of BrdU-incorporating cells was calculated. The mock-treated control was assigned as 100% proliferative.

For **ß-Galactosidase activity** at pH 6 detectable 72 h post-irradiation, Sigma-Aldrich Senescent Cells Staining Kit was used. Cells were washed (1 ml PBS, 2x) and fixed with 1.5 ml per well 1x fixation buffer (dil. 1:10 with ultrapure ddH_2O) for 7 min at RT. After removal of the fixation buffer, the cells were washed again (1 ml PBS, 3x) and submerged with 1 ml filtered (0.2 µm) ß-galactosidase assay staining mixture per well. The plates were sealed with Parafilm and incubated at 37°C in a CO_2-free incubator for 16 h. After incubation, the ß-Galactosidase-positive cells were counted under bright field and displayed as % of total cell number (protocol analogous to Debacq-Chainiaux 2009)[45].

3. 3 UV-RHE

3. 3. 1 Establishment of 3D reconstructed epidermis

To build the constructs, UV-B-irradiated and mock-treated keratinocytes were removed from the wells and again centrifuged at aforementioned conditions. The cells were resuspended in 400 µl basal medium and seeded into cell culture inserts at 3 x 10^5/cm^2. The inserts were placed in a fresh 6-well plate and submerged with 3.2 ml basal medium to allow monolayer formation. The plates were kept in a 5% CO_2 incubator at 37 °C for 48 h. Before airlift, the monolayers were soaked in differentiation medium for another 24 h. The basal medium was removed thoroughly and replaced with 400 µl differentiation medium inside and 3.2 ml outside the inserts. After 24 h, the constructs were lifted to the air-liquid interface. They were supplied with 2 ml differentiation medium submerging the inserts from the outside only. The plates were kept in 5% CO_2 and 37°C for 14 days with medium changes every 2-3 days, to allow full stratification of the constructs.

3. 3. 2 Relative gene expression by RT-qPCR

RNA isolation

Total RNA was isolated from the constructs at day 14. Cells were lysed with 350 µl buffer RA1 and 3.5 µl ß-mercaptoethanol at 11.000 rpm for 1 min at RT using NucleoSpin RNA II kit. Briefly, the lysate was filtered through a NucleoSpin filter for 1 min at 11.000 rpm, mixed with 350 µl 70% ethanol and loaded onto a NucleoSpin RNA II column, then centrifuged for 30 sec at 11.000 rpm. After desalting the membrane with 350 µl membrane desalting buffer for 1 min at 11.000 rpm, the membrane was washed in three centrifugation steps at 11.000 rpm (1^{st}: 200 µl buffer RA2, 30 sec, 2^{nd}: 600 µl buffer RA3, 30 sec; 3^{rd}: 250 µl buffer RA3, 2 min). The RNA was eluted in 60 µl RNAse-free H_2O at 11.000 rpm for 1 min.

DNA digestion

Remaining DNA was removed by DNA digestion. For each reaction, 8 µl of RNA isolate were added to 1 µl 10x reaction buffer and 1 µl DNAse I (amplification grade) and incubated for 15 min at RT. 1 µl 50 mM EDTA were added to bind calcium and magnesium ions and inactivate DNAse I. The reaction mix was heated to 70°C for 10 min in the Thermocycler, then cooled to 4°C.

First Strand cDNA synthesis

10 µl of purified RNA were added to 9 µl of the master mix. The reaction mix was incubated in the thermocycler for 5 min at 25°C, followed by 60 min at 42°C and 5 min at 70°C, then cooled on ice. 20 µl cDNA were diluted with 60 µl DEPC-treated H_2O.

RT-qPCR

RT-qPCR was performed in 96-well plates. Each reaction consisted of 1 µl corresponding forward- and 1 µl reverse primer and 2 µl of cDNA template. No-template controls were performed for each gene with 2 µl H_20 instead of template. The sealed 96-well plate was inserted to a LightCycler 400. The program consisted of 45 cycles with denaturation at 94 °C for 10 sec followed by annealing at 60 °C for 10 sec and extension at 72°C for 10 sec. Amplification was terminated with extension at 72 °C for 10 min. Relative mRNA amounts of samples were calculated using the ΔCt method ($2^{\Delta Ct = Ct \text{ of the target} - Ct \text{ of the reference}}$). Reference gene was Glyceraldehyde 3-phosphate dehydrogenase (GAPDH).

3. 3. 3 Measurement of cytokines in culture medium

Medium (2 ml) from outside the inserts was collected at day 2 (7, 14) of the cultivation period with 48 h between medium changes. Cytokine levels for IL-1α (IL-6, -8, -12, TNFα) were determined with colorimetric ELISA. A 96-well plate was coated with 100 µl per well of the capture antibody diluted in reagent diluent (IL-1α, IL-6: 2.0 µg/ml; IL-8, IL-12, TNFα: 4

µg/ml) and incubated overnight at RT. The next day, the plate was washed (wash buffer, 3x) and blocked with 300 µl per well block buffer for 1 h at RT. After repeated washing (wash buffer, 3x), the plate was coated with 100 µl of the appropriate sample or solution of the appropriate standard (Std 1: IL-1α: 500 pg/ml; IL-6: 600 pg/ml; IL-8, IL-12: 2000 pg/ml; TNFα: 1000 pg/ml) per well and incubated for 2 h at RT. After repeated washing (wash buffer, 3x), the plate was now coated with 100µl solution of the appropriate detection antibody diluted in reagent diluent (IL-1α, IL-6: 50 ng/ml; IL-8: 20 ng/ml, IL-12: 100 ng/ml, TNFα: 250 ng/ml) per well and incubated for 2 h at RT. After repeated washing (wash buffer, 3x), 100 µl working dilution of streptavidin-HRP (dil. 1:200 in reagent diluent) were added to each well, followed by incubation for 20 min at RT in the dark. After washing (wash buffer, 5x), 100 µl substrate solution per well were added and incubated for 20 min at RT in the dark. The reaction was stopped with 50 µl stop solution per well and the absorption at 450 nm was measured in a FluoStar microplate reader.

3. 3. 4 Western Blotting

Cell lysis and protein isolation

Epidermis equivalents were cut out of the inserts, transferred to an Eppendorf tube with 247.5 µl pre-cooled RIPA basal buffer and 2.5 µl proteinase-phosphatase inhibitor cocktail and a steel bead to help lyse the tissue. The tube was moved to a tissue lyser and treated at 25 Hz for 2 min, followed by incubation on ice for 15 min. Afterwards, the contents of the tube were centrifuged in a mini centrifuge for at 10.000 rpm for 1 min. To complete the protein isolation, the tubes were centrifuged for 30 min at 13200 rpm and 4°C. The supernatant was transferred to a new tube.

Protein quantification

Pierce BCA Protein Assay Kit was used to determine total protein content of the samples. Samples were adjusted to contain 20 µg of protein each to assure equal loading amounts in preparation for loading of the SDS gel. A standard curve of bovine serum albumin was prepared with 2000 µg/ml as highest and 25 µg/ml BSA as lowest standard. 7.2 ml working reagent were prepared by mixing 7.056 ml reagent A with 0.144 ml reagent B (50:1, reagent

A : B). 25 µl of standard or sample per well were added to a 96-well-plate together with 200 µl working reagent, briefly vortexed and incubated for 30 min at 37°C. Absorption was measured at 562 nm.

Preparation of samples and protein markers for electrophoresis:
30x DTT solution was diluted 10:1 with 3x loading buffer. The appropriate volume containing 20 µg protein was mixed 2:1 with loading buffer-DTT. After heating at 95°C for 5 min, samples were cooled on ice and micro-centrifuged for 5 min at 11000 rpm and 4°C. 30 µl of the prestained protein Western-C Precision Protein marker were heated at 95°C for 5 min, shortly microcentrifuged and loaded onto the gel. 20 µl of biotinylated protein marker were heated at 95°C for 2 min, shortly microcentrifuged and loaded onto the gel. Immediately after addition of APS, 10 ml of the solution was filled in between the glass plates and overlaid with 1 ml isopropanol until polymerization. Isopropanol was removed from the running gel surface. Immediately after addition of APS, 3 ml stacking gel was mounted together with the comb until polymerization.

Electrophoresis and protein transfer

The lower reservoir of the electrophoresis chamber was filled with running buffer, the plates were mounted, then the upper reservoir was filled with the buffer and the comb was removed. The slots were washed (running buffer, 1x) and samples or protein markers were added. The gel was run at 150 V for 1 h, then washed with transfer buffer for 15 min and put onto a pretreated PVDF membrane (Methanol, 15 sec; ddH_2O, 2 min; transfer buffer, 5 min). The blot sandwich was placed into the semi-dry blotting unit. The blot was run at standard program for 15 min.

After transfer, the membrane was bathed for 10 sec in methanol, then air-dried for 15 min on tissue paper, rehydrated for 10 sec in methanol and rinsed in ddH_2O. The membrane was incubated in 25 ml block buffer for 1 h at 37°, then washed (15 ml TBST, 5 min, 3x). The membrane was incubated with the primary antibody diluted to 10 ml block buffer (anti-ß-actin 1: 1000, anti-ß-galactosidase 1:250) overnight at 4°C under agitation, then washed (5 ml TBST, 5 min, 3x). Then, the membrane was incubated with the secondary antibody diluted

to 10 ml block buffer (anti-ß-actin, 1:1000; anti-biotin HRP-conjugated antibody, 1:5000) for 1 h at RT under agitation, followed by washing (15 ml TBST, 5 min, 3x). The membrane signal was developed by addition of SignalFire ECL reagent at different exposure times (30, 60, 120 sec) and viewed in the detection chamber connected to computer software. In case of stripping of the membrane, the blot was incubated with preheated stripping buffer at 50°C for 30 min, then washed (1x TBST; 3x) and re-blocked.

3. 3. 5 Histology

For cryoembedding at day 14, the constructs and supporting membranes were cut out from the plastic inserts with a sterile blade and submerged in OCT medium in 25 x 2 x 5 mm vinyl specimen molds, frozen in liquid nitrogen and stored at –80°C. The specimen were cut into 10 µm slices and transferred onto polylysine slides.

For hematoxylin and eosin (H&E) staining, the slides were air-dried for 30 min and fixed with 4% paraformaldehyde Roti-Histofix for 7 min at RT. The slides were immersed in ddH_20 and submerged in Mayer's hematoxylin solution for 5 min with agitation. After washing with tap water for 5 min with agitation, the slides were submerged in 0.5% eosin Y solution for 30 sec followed by subsequent dehydration steps in 96% (2 min., 2 x) and 100% (2 min, 2 x) ethanol. The stained slides were then submerged in RotiHistol (2 min, 2x) and air-dried for 20 min, mounted in RotiHistokitt mounting medium and analyzed under bright field microscopy.

For immunofluorescence, slides were air-dried for 30 min at RT and fixed with 4% paraformaldehyde Roti-Histofix for 7 min at RT. The slides were washed (PBS, 1 x; 0.0025% BSA + 0.025 % Tween 20, 1 x) and blocked with primary goat serum (1:20 in PBS) for 30 min at RT. The slides were submerged in 400 µl primary antibody solution (anti-Vinculin, -γH2AX, Keratin 10, -Involucrin, -Claudin-1, -Filaggrin, -Keratin 14 dil. 1:200 to 0.0025% BSA + 0.025 % Tween 20) and incubated overnight at 4 °C. The slides were then washed (0.0025% BSA + 0.025 % Tween20, 3 x) and incubated with secondary antibody solution (goat anti-mouse 594 DyLight dil. 1:400 to 0.0025% BSA + 0.025 % Tween 20 for 1 h at RT in the dark. After washing (0.0025% BSA + 0.025 % Tween 20, 3 x), the slides were mounted with DAPI

mounting medium and analyzed by fluorescence microscopy (filter excitation wavelength 594 nm). Negative controls were treated according to the protocol without primary antibody. Exposure times were adjusted for the negative controls to give no signal at expected wavelength.

Measurement of epidermal thickness

H&E stained sections were viewed under bright field microscope (20 x). Thickness in µm of viable epidermis (VE) and stratum corneum (SC) was measured by two-point measurement. Three pictures per sample were taken. In every picture, VE and SC were measured two times, one on the right and one on the left side of the picture for a total of six measurements per stratum (VC and SC) and sample. Means of six measurements were calculated for both stratae and depicted in µm thickness.

Keratinocyte count

Numbers of cells in 10 µm sections of normal and UV-RHE were automatically counted by Image J software after transformation of the pictures of DAPI-stained cell nuclei into binary 8-bit images. Three images for every sample were analyzed and the mean was determined.

Quantification of DNA-damage marker γH2AX

Numbers of γH2AX-positive cell nuclei were normalized against the total cell number per image (counted by Image J software after transformation into binary 8-bit images). γH2AX-positive nuclei per image were manually counted by an unbiased observer under fluorescence microscope and normalized to the total cell nuclei number per image. Three images of every sample were analyzed by this method of a total of 5 donors. Of the normalized numbers of γH2AX-positive cells, the mean of three images was calculated and depicted as % γH2AX-positive cell nuclei per total cell nuclei number.

3. 3. 6 Permeation of radioactively labeled testosterone and caffeine

Permeation of the constructs was tested in the plastic inserts placed in 6-well plates. Prior to the experiment, the culture medium was replaced with PBS (1.5 ml) pre-warmed to RT. The constructs were left to equilibrate for 30 min in 5 % CO_2 at 32°C. After 30 min, 200 µl sample (t=0) was retrieved from the acceptor medium. 150 µl donor medium (40 µg/ml 1,2,6,7-^{3}H-Testosterone in PBS with 2% (v/v) Igepal or 1 mg/ml ^{14}C caffeine in PBS) was applied onto the construct. The applied donor solution was adjusted to an activity of 2 µCi for both substances. The plate was placed into the incubator. After 30 min, 200 µl sample (t=1) was retrieved, 30 min later again (t=2) and so forth for the next 3 (6) h. The acceptor medium was thoroughly mixed by pipetting up and down six times before retrieval of each sample. After each sample, the retrieved volume was replaced with 200 µl RT PBS. After sample t=6 (t=12), 200 µl sample or standard were added to 1 ml scintillation cocktail and measured in a Beta-Counter (scintillation counter). P_{app} values were calculated.

3. 3. 7 Penetration of Nile red loaded to CMS nanocarriers and of ICC-tagged CMS nanocarriers

80 µl (finite dose approach) of an aqueous solution of CMS nanocarriers loaded with Nile red (5g/L) kindly provided by SFB project A01 (M. Unbehauen, AG Prof. Haag) were applied onto the constructs, then kept at 37 °C 5% CO_2 for 3 (6) h. Then, the medium was collected and the constructs were cut out of the inserts, embedded in tissue freezing medium and frozen in liquid nitrogen. 10 µm cryosections of the epidermis constructs on slides were air-dried for 30 min, then viewed under bright field and fluorescence (red, filter excitation wavelength) to obtain an overlay picture of both channels.

The analogous method was used to analyze the penetration of CMS nanocarriers tagged with indocarbocyanine (ICC) (5g/L, also provided by project A01). In the conventional fluorescence microscopy analysis, arbitrary brightness units (ABU) quantified the fluorescence intensity in different stratae: 2 x 100 pixel lines were placed into the stratum corneum and viable epidermis. In every picture, VE and SC brightness were quantified in this manner two times, one on the right and one on the left side of the picture for a total of six

measurements (3 images per sample). The means of six measurements were calculated and depicted in Mean ± SEM ABU for both stratae.

Trace analysis indocarbocyanine (ICC)

To confirm that the epidermis constructs have a closed monolayer and no CMS-ICC nanocarriers when applied onto the surface permeate into the culture medium, the collected medium was analyzed for subtle color changes. After 3 or 6 h exposure of the constructs to the CMS-ICC nanocarriers, the culture medium (2 ml) was harvested and stored at -80 °C for color analysis. For reference, 90 µl CMS-ICC nanocarriers were added to 2 ml medium. From this starting concentration, a dilution series was made with 1 µl CMS-ICC nanocarriers in 2 ml medium as the lowest dilution. Next, absorptions of the diluted solutions were determined at 540 nm in a photometer. In the same experiment, media collected from 3 and 6 h penetration studies were measured. Absorption values of culture medium collected from the penetration experiments were compared to absorptions of the dilution series. Additionally, 80 µl CMS-ICC nanocarriers were applied directly onto insert membranes without the constructs for 20 min to test if CMS-ICC nanocarriers can move through the pores of the membrane.

FLIM analysis of CMS-ICC nanocarrier penetration

Much more sensitive analysis of nanocarrier penetration via FLIM (Fluorescence Lifetime Imaging Microscopy) was enabled through cooperation with SFB 1112 Project B03. Cryosections (10 µm) of reconstructed epidermis treated with CMS-ICC nanocarriers for 3 (6) h and untreated constructs were placed on 0.17 mm thick cleaned cover glasses and subjected to FLIM [66, 67]. Time-correlated single photon counting using a confocal laser scanning FLIM setup allowed establishing time-resolved fluorescence decay curves for each image pixel. The FLIM images were analyzed by self-written routines in C++. The partition into classes (clusters) of the fluorescence decay curves was performed with the use of a multivariate pattern recognition method. Fluorescence decay values of the different clusters were fitted with a sum of exponentials using x^2 minimization. Next, false-color images were

generated: a discriminative color was assigned to every pixel containing the fluorescence decay curve corresponding to one cluster [64].

3. 4 Statistical analysis

Mean values of independent experiments are represented with SEM (standard error of the mean). “n” is the number of donors (number of biological replicates). Data was analyzed using *Kruskal-Wallis* one-way ANOVA and Dunn’s post hoc test (*$p \leq 0.01$; $p \leq 0.05$).

4 Results

4. 1 Keratinocyte monolayers

4. 1. 1 UV-B induced senescence in keratinocytes

The additional expression of ß-galactosidase at pH 6 (regular ß-galactosidase expression in proliferative cells is at pH 3-4) is an exclusive marker of senescent cells. The senescence-associated ß-galactosidase (SA-ß-galactosidase) can be made visible through a colorimetric pH-dependent assay **(Fig. 1A)**. Single-doses of UV-B light (9.6, 23.7, 25, 30 mJ/cm^2) were applied to primary human keratinocytes from juvenile foreskin and tested for the expression of senescence-associated ß-galactosidase.

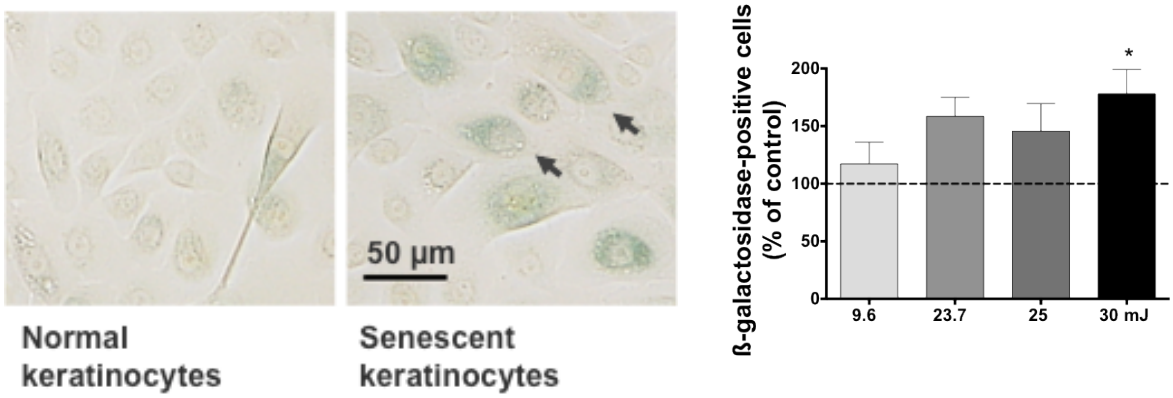

Fig. 1: UV-B irradiation induces senescence in juvenile keratinocytes. A) Irradiated cells were stained for ß-galactosidase activity at pH 6 (green) in response to different UV-B doses after 72 h. Morphology of ß-galactosidase-positive keratinocytes corresponds to typical features of senescent cells. Arrows highlight typical enlarged cell. B) Numbers of ß-galactosidase-positive stained cells were normalized to the total cell number and expressed as % of the positive cells of the non-irradiated control. Magnification: 10x. Mean ± SEM, n=5-6. *$p \leq 0.05$.

An increase in senescence-associated ß-galactosidase-expressing keratinocytes was observed with irradiation **(Fig. 1B)**. Up to 50% increase compared to positive-stained cells in the non-irradiated control (0 mJ/cm^2) was seen for 25 mJ/cm^2 UV-B. A moderate increase was seen for the lower dose of 9.6 mJ/cm^2. Higher doses (30 mJ/cm^2) resulted in a 75 % increase in ß-galactosidase-positive keratinocytes in monolayer experiments, but these cells

did not lead to constructs with correct monolayer formation. Therefore, cells exposed to UV-B 25 mJ/cm^2 and 9.6 mJ/cm^2 were used for the construction of UV-RHE. In terms of morphology, the ß-galactosidase-positive cells matched the senescent cell phenotype **(Fig. 1A)**: 1) enlarged, flattened, 2) increased nuclei size, and 3) strong vacuolization and granulation. This observation indicated that the chosen UV-B doses were suitable to induce premature, stress-induced senescence.

4. 1. 2 UV-B effect on keratinocyte viability and proliferation

The DNA damage response to UV-B irradiation can take up to 72 h after stimulus to fully develop. To investigate UV-induced mortality, keratinocyte viability was tested over time **(Fig. 2)**. A dose of 25 mJ/cm^2 UV-B decreased the viability by 25% after 48 h and by 30% after 72 h. This suggested that the cell viability was reduced in a time-delayed fashion. The lower dose (9.6 mJ/cm^2) was less toxic, here, the viability declined by 20 % after 72 h.

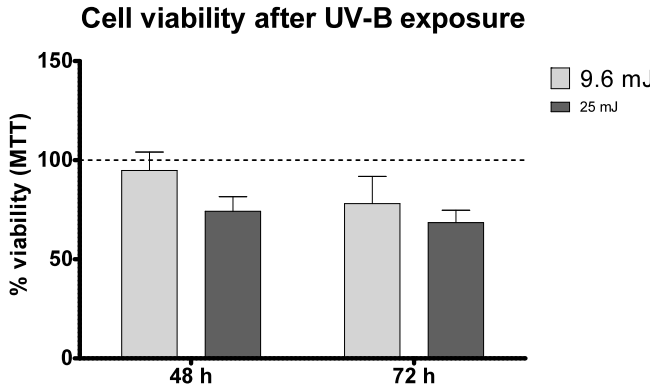

Fig. 2: Keratinocyte viability is reduced in response to UV-B exposure. Keratinocytes were irradiated and viability was measured by MTT test. Absorbance (540 nm) of the non-irradiated control and the UV-B treated samples was analyzed 48 (72) h post-irradiation. Non-irradiated controls are assigned as 100 % viability. Mean ± SEM, n=5.

Next, the proliferation of irradiated keratinocytes was tested **(Fig. 3)**. No reduction of proliferation was found after 24 h. After 72 h, the proliferation of cells treated with 25 mJ/cm^2 was reduced by 25 %. The proliferation of cells treated with 9.6 mJ/cm^2 remained at control level. It is concluded that the UV-B effect on proliferation of human juvenile keratinocytes is both dose- and time-dependent. A time-delayed decline in the numbers of proliferative cells was in accordance with the DNA damage response (growth arrest followed by apoptosis or senescence) post-stimulus.

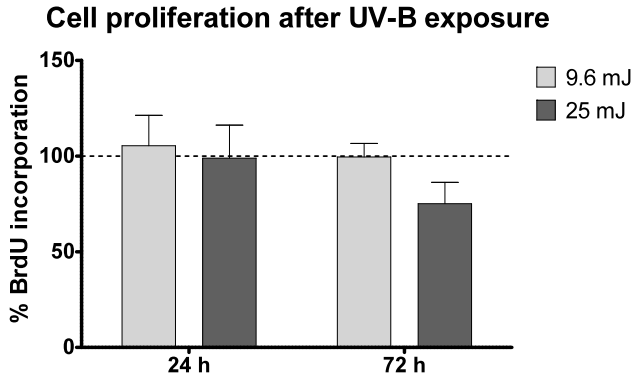

Fig. 3: Proliferation of keratinocytes irradiated with 25 mJ/cm^2 UV-B declines after 72 h. Keratinocytes were irradiated with UV-B doses (9.6, 25 mJ/cm^2). Incorporation of the thymidine analogue BrdU 24 (72) h post stimulus was measured by absorbance at 450 nm. The non-irradiated controls were assigned as 100%. Mean ± SEM, n=5.

4. 2 UV-RHE

UV-B irradiated keratinocytes were used to construct UV-RHE while non-irradiated keratinocytes of the same batch were used in parallel for normal RHE **(Fig 4)**. The irradiated keratinocytes and the non-irradiated (mock-irradiated) control keratinocytes developed a stratified epidermis after 14 days (post-airlift) of cultivation with intermittent medium changes.

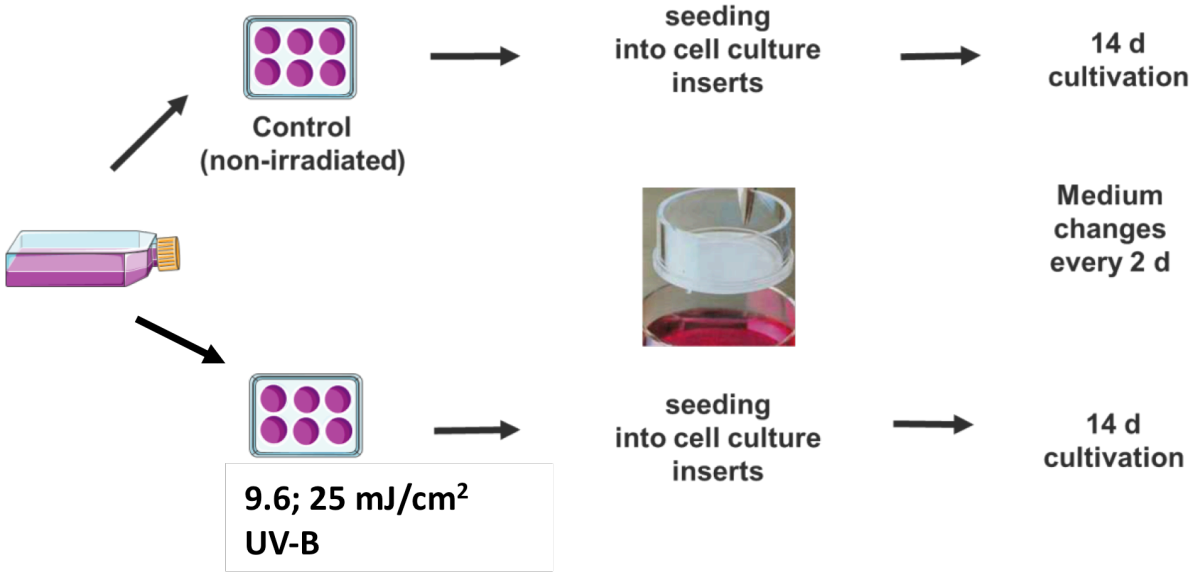

Fig. 4: Construction of an epidermis model from UV-B irradiated keratinocytes. Juvenile keratinocytes from foreskin were grown to 80% confluency at passage 2. They were detached from the flasks and transferred to 6-well-plates at 3x10^5 cells/well, then irradiated and immediately seeded into cell culture inserts (12 mm diameter, 0.4 µm pore size, polycarbonate membrane).

4. 2. 1 Morphology

The normal RHE displayed a correct epidermal basal layer with typical erect keratinocytes **(Fig. 5: a,c)** and round-shaped nuclei. Histology corresponded to human epidermis *ex vivo.* The well-developed stratum spinosum consisted of 3-5 viable layers with regularly shaped, horizontally aligned keratinocytes. The stratum granulosum was clearly visible by an alignment of flat, dark staining cells, **(Fig. 5: b)** typical for the basophilic keratinocytes found at the stratum granulosum of human epidermis *ex vivo*. Interestingly, indications to

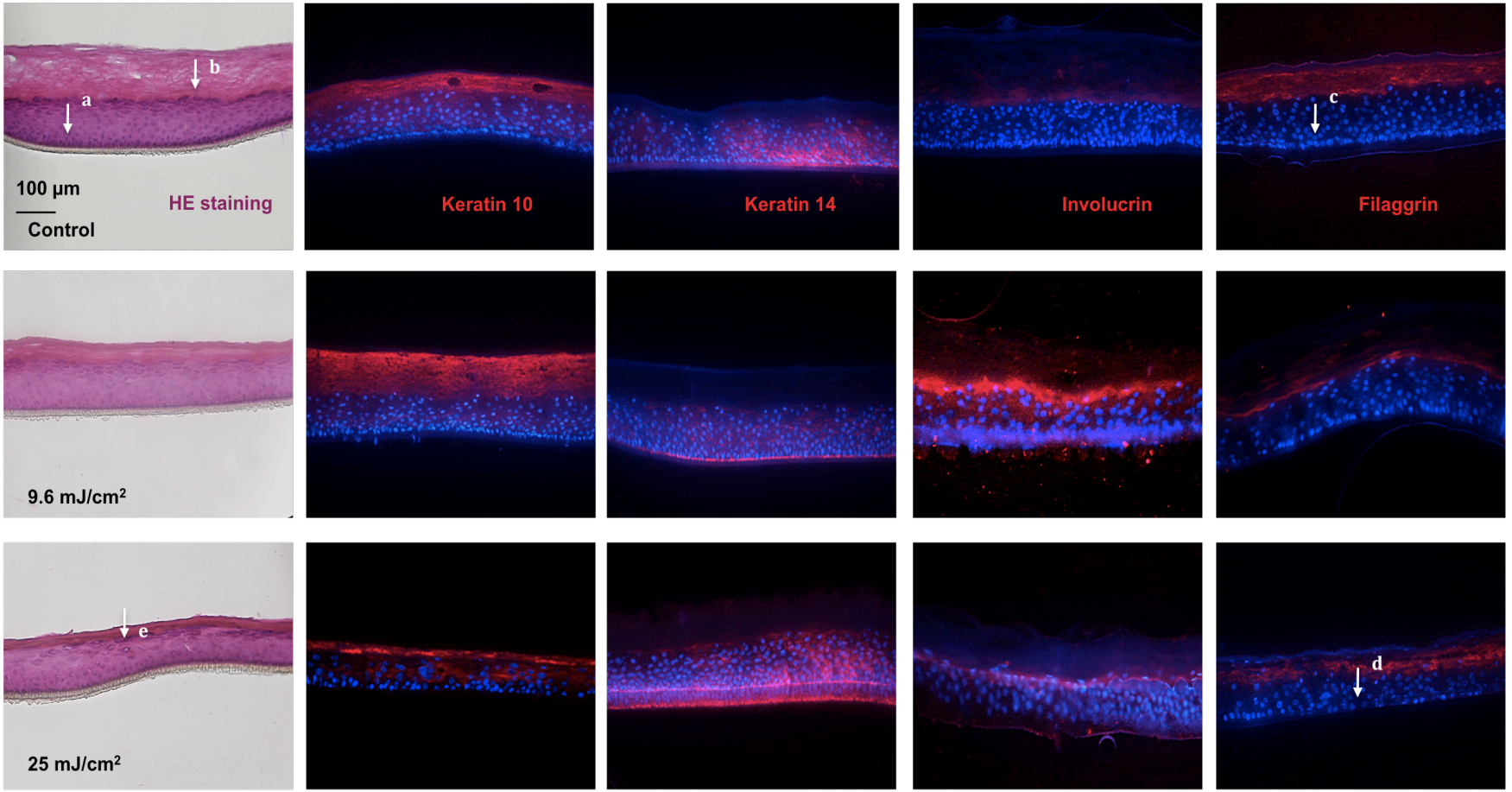

Fig. 5: UV-B irradiated keratinocytes and control cells form a stratified epidermis after 14 d cultivation. Keratinocytes were irradiated with UV-B prior to seeding on a polycarbonate membrane. Mock-treated keratinocytes and irradiated keratinocytes were cultured for 14 days post-airlift with intermittent medium changes. 10 µm cryosections were HE-stained for morphology and immunostained for expression of early (keratins 10, 14) and late (involucrin, filaggrin) differentiation markers (red). Cell nuclei were stained with DAPI (blue). Magnification: 10x. Pictures are representative of RHE built from the cells of 3-6 donors.

parakeratosis, which is a common problem in RHE, were absent. Keratinocytes of the basal lamina in 25 mJ/cm^2 UV-RHE were disorganized, with horizontal orientation and irregular spaces between neighboring cells **(Fig. 5: d)**. Differences were also obvious in the stratum spinosum: while the control construct showed a regular pattern of nuclei with dense alignment of the cells, the 25 mJ/cm^2 construct showed a disturbed pattern. The stratum granulosum was hyperchromatic and showed signs of acantholysis by comparison to the constructs from non-irradiated keratinocytes **(Fig. 5: e)**.

The constructs from keratinocytes irradiated with 9.6 mJ/cm^2 were in part similar to the control and in part similar to 25 mJ/cm^2 constructs. To some degree, irregularities of the basal membrane could be observed, similar to 25 mJ/cm^2 constructs. The stratum corneum was uneven and appeared thicker in some constructs and thinner in others. Interestingly, the amount of stratum corneum was intermediate between control and 25 mJ/cm^2 construct **(Fig. 6)**. The same applied to the total thickness of 9.6 mJ/cm^2 UV-RHE (measured from the basal layers to the stratum corneum).

The early differentiation markers Keratin 10 and 14 were expressed in all constructs from UV-B irradiated and non-irradiated keratinocytes **(Fig. 5)**. In normal human epidermis, the early differentiation marker keratin 14 is expressed in all viable layers and the basal lamina [17]. This was also the case in UV-RHE and normal RHE. Keratin 10 is normally restricted to the suprabasal layers while the basal lamina remains negative. This pattern could be confirmed for all constructs, too. The late differentiation markers, involucrin and filaggrin, indicated complete maturation of the epidermis **(Fig. 5)**. Involucrin and filaggrin are expressed predominantly in the upper layers at the transitional phase of stratum granulosum and stratum corneum. In RHE, contrary to human epidermis *ex vivo*, involucrin may be detectable also in the suprabasal layers while filaggrin is restricted to the uppermost layers [69]. Here, the broader pattern of involucrin distribution was observed for the UV-RHE, while the control construct expressed involucrin only in the uppermost layer. Filaggrin was expressed with appropriate localization in all the constructs (9.6, 25 mJ/cm^2 and control).

4. 2. 2 Thickness of stratum corneum and viable epidermis

The most obvious difference between constructs from irradiated and non-irradiated keratinocytes was the stratum corneum: both 9.6 and 25 mJ/cm^2 UV-RHE clearly had thinner stratum corneum than the normal RHE, as determined by measurement of the thickness **(Fig. 6B)**. The effect was significant in 25 mJ/cm^2 UV-RHE ($p \leq 0.01$). Also the thickness of the viable epidermis was reduced, but the difference was not as striking. Interestingly, the 9.6 mJ/cm^2 UV-RHE showed a reduction in thickness of stratum corneum intermediate between control and 25 mJ/cm^2 UV-RHE. To gain more insight, the influence of seeding numbers on the morphology was tested **(Fig. 6A, upper panel)**. Non-irradiated keratinocytes were seeded into inserts at standard numbers (3 x 10^5 cells/cm^2) and reduced numbers (2 x 10^5 and 1.5 x 10^5 cells/cm^2). After 14 days, the morphology was compared. Even a 50 % reduction of the standard seeding density resulted in reconstructed epidermis with normal histology. The ratio of stratum corneum to viable layers was clearly unchanged. Thus, the reduced epidermal layers of the UV-RHE **(Fig. 6A, lower panel)** were not caused by fluctuations in the seeding numbers. Also, the total keratinocyte count per 10 µm section **(Fig. 6C)** was relatively constant in normal and UV-RHE, indicating that the reduction of the layers resulted from flattened and/or exfoliated corneocytes.

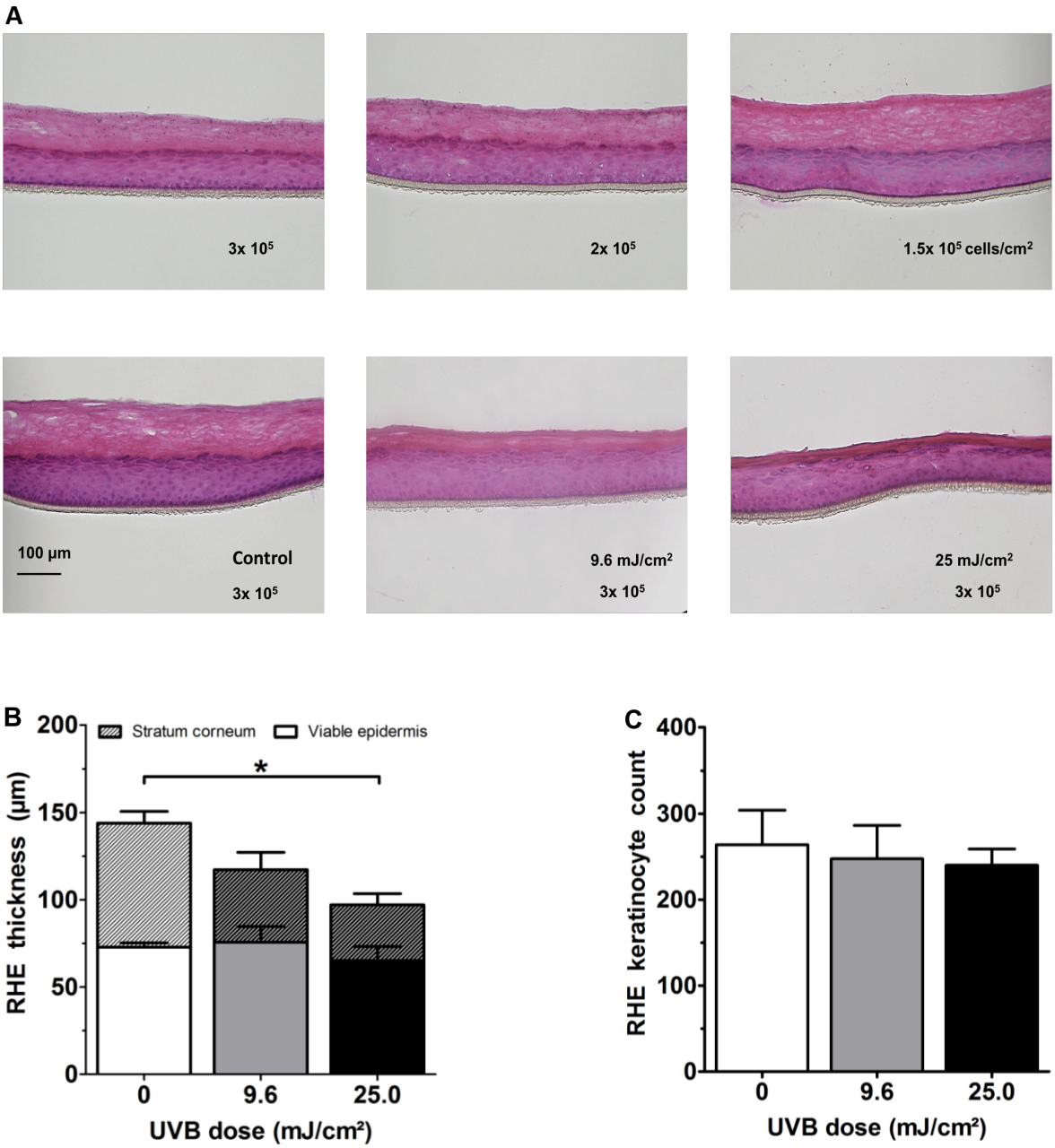

Fig. 6: A) Number of seeded cells does not change the stratum corneum of reconstructed epidermis. Non-irradiated, juvenile keratinocytes ($3x10^5$ cells/cm^2) and ($2x10^5$ and $1.5x10^5$ cells/cm^2), respectively, were seeded on polycarbonate membranes and cultivated for 14 d post-airlift. 10 µm cryosections were HE-stained to compare morphology of the constructs. Magnification: 10x. Pictures are representative of two (upper panel) and 6 (lower panel) donors. B) Measurement of epidermal thickness in normal and UV-RHE. Mean ± SEM, n=5. *$p \leq 0.01$. C) Numbers of keratinocytes per 10 µm cryosections of normal and UV-RHE. Mean ± SEM, n=5.

4. 2. 3 Tight-Junction proteins

The adequate expression of tight-junction proteins, providing the close net of cell-cell contact, is crucial for the functionality of the epidermal barrier. The expression of claudin-1, an important tight junction protein [49], was detected in all constructs **(Fig. 7)**. This indicates that tight junctions are expressed in this type of RHE, as had also been shown for another of our in-house constructs, a full-thickness skin model [70].

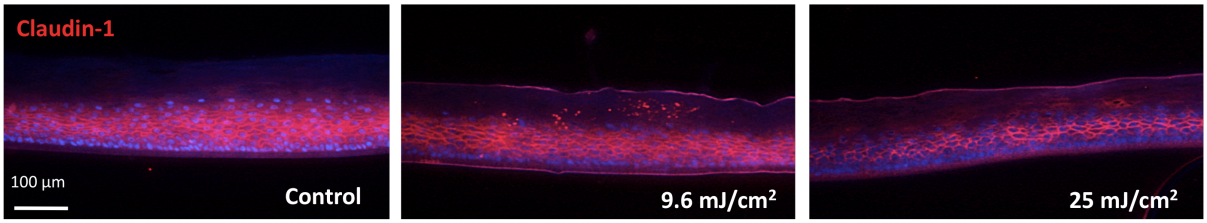

Fig. 7: Staining of tight junction protein claudin-1. 10 µm cryosections were immunostained with an antibody to TJ protein claudin-1 (red). Cell nuclei were stained with DAPI. Magnification: 10x. Pictures are representative of at least three donors.

It was reported before that UV-B irradiation leads to deterioration of tight junction proteins in cultured keratinocytes and human skin so that the barrier function becomes less functional [48]. Here, the staining of TJ proteins in UV- and normal RHE did not confirm this observation. Still, functional alterations of the barrier in UV-RHE were then investigated more closely by the permeation of the OECD standard compounds.

4. 2. 4 Expression of ß-galactosidase in UV-RHE

As mentioned before, the additional activity of ß-galactosidase at (suboptimal) pH is an exclusive biomarker of senescent cells [42]. Interestingly, it was demonstrated by Kurz et al. [44] that senescence-associated ß-galactosidase activity also correlates with higher total ß-galactosidase protein content. Western Blotting was used to detect ß-galactosidase in tissue lysates from normal and UV-RHE **(Fig. 8)**.

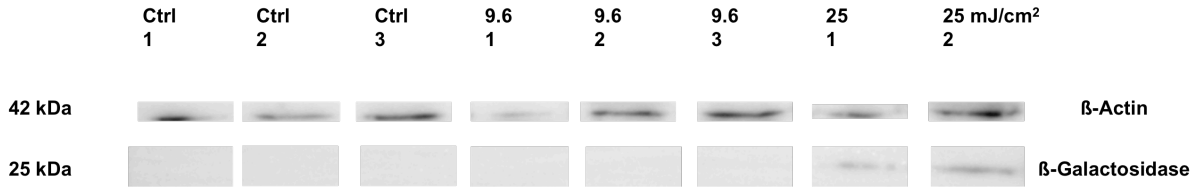

Fig. 8: 25 mJ/cm^2 constructs display detectable amounts of senescence marker ß-galactosidase. Tissue lysates were tested for expression of ß-galactosidase and housekeeping protein ß-actin by SDS gel electrophoresis and Western Blotting. BCA protein quantification was used to ensure equal protein content in all samples (20 µg). Protein bands are representative of two (25 mJ/cm^2) to three (9.6 mJ/cm^2 and control) donors.

UV-RHE from keratinocytes irradiated with 25 mJ/cm^2 was positive for ß-galactosidase expression (25 kDa) **(Fig. 8)**. This was the case for reconstructed epidermis from two donors and reflects increased ß-galactosidase content in these samples. The signal was negative in 9.6 mJ/cm^2 and control constructs, which is ascribed to the detection limit of the Western Blot. The positive ß-galactosidase signal strongly suggests an increased number of senescent cells in the respective constructs. This is in line with an increased number of senescent cells in aged skin *in vivo* [71].

4. 2. 5 Secretion of cytokines

To investigate if UV-B irradiation influences baseline cytokine secretion of the epidermis constructs, the culture medium was harvested at day 2, 7 and 14 and the pro-inflammatory cytokines (IL-1α, IL-6, IL-8, IL-12, TNFα) which are part of the secretome of senescent cells (SASP) [24], but are also induced in response to UV-B irradiation, were quantified by ELISA **(Fig. 9)**.

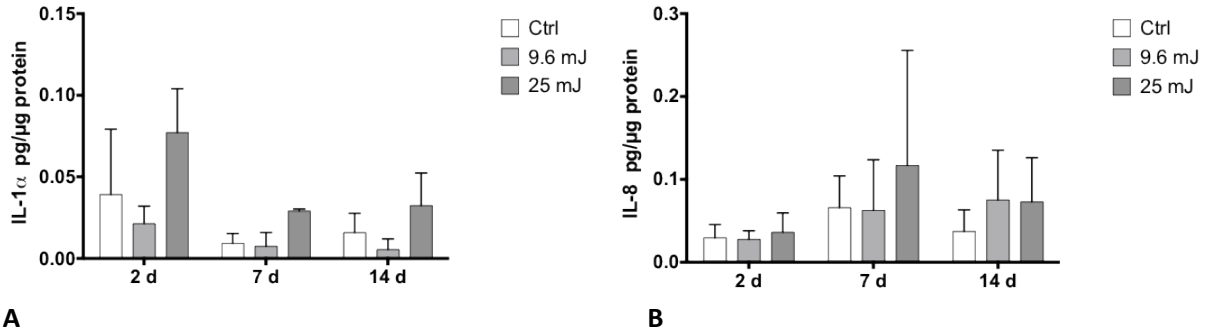

Fig. 9: IL-1α and IL-8 secretion of reconstructed epidermis throughout 14 d of cultivation. Culture media of reconstructed epidermis were harvested at day 2, 7 and 14. Intervals between medium changes were 48 h. Cytokine levels of A) IL-1α and B) IL-8 were determined with ELISA and normalized to total protein content of the constructs. Mean ± SEM, n=3 (IL-1α), n=6 (IL-8).

Levels of IL-1α **(Fig. 9A)** fluctuated but were highest at day 2 in all constructs. There was a lightly increased secretion of IL-1α in 25 mJ/cm^2 UV-RHE compared to 9.6 mJ/cm^2 and control RHE at all time points, indicating a pro-inflammatory effect of the UV-B irradiation. Variations were due to the high susceptibility of IL-1α to degradation. The increased IL-1α levels preceded the increased IL-8 levels from day 7 until day 14. Elevated levels of IL-8 **(Fig. 9B)** were detected in 25 mJ/cm^2 constructs 14 days post-stimulus. IL-8 is secreted as an acute response to UV-B irradiation with a maximum 24 to 48 h following the irradiation. Thus, the high IL-8 level detected 14 days after the UV-B stimulus does not represent an acute effect, but rather represents a long-term consequence of the irradiation. The cytokine levels of the UV constructs exceeded those of the non-irradiated constructs about twofold throughout.

IL-6, IL-12, and TNFα concentrations were below the detection limit of the ELISA. The results indicate that these cytokines are either not secreted or not adequately detected due to their low concentration in the culture medium, which was of large volume (2 ml) in relation to the construct surface (1 cm^2).

4. 2. 6 Gene expression

Several crucial regulators of the cell cycle are associated with up- or downregulation in senescent cells. To investigate whether differences in the regulation are reflected on the gene expression of normal and UV-RHE, cDNA of RNA isolated from the tissue lysates was analyzed via RT-qPCR **(Fig. 10)**.

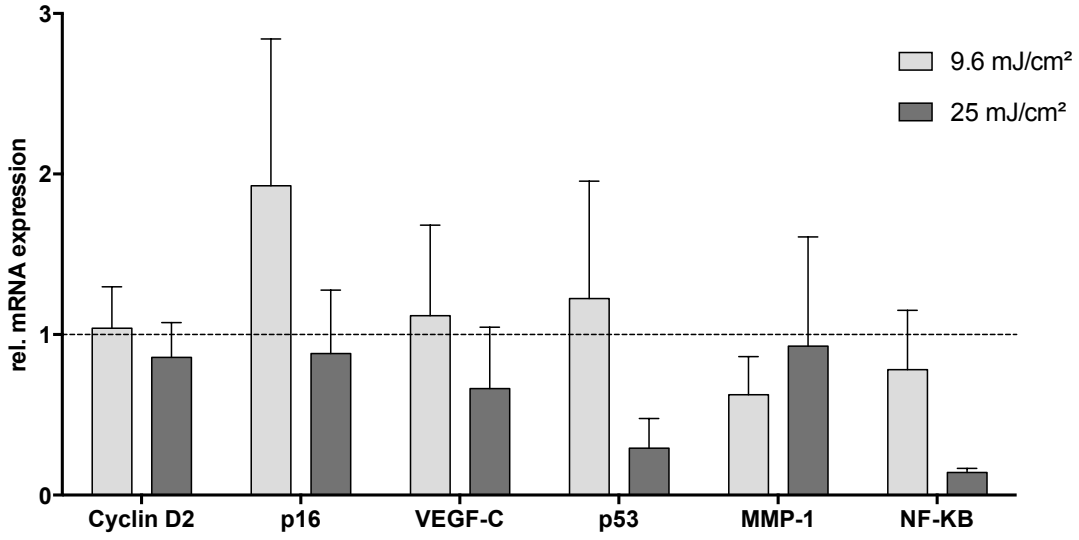

Fig. 10: Relative gene expression of senescence-associated genes. mRNA was isolated from reconstructed epidermis tissue lysates at day 14 and converted to cDNA. Expression of target genes relative to housekeeping gene GAPDH was determined by RT-qPCR. Control (normal RHE) expression is assigned as 1. Mean ± SEM, n=3-5

One negative, $p16^{ink4a}$and one positive regulator of the cell cycle, cyclinD2, were analyzed. $p16^{ink4a}$ expression suppresses DNA synthesis. Its expression is necessary when cells are arrested in the G1-phase of cellular division (required for senescence) [72, 73]. $P16^{ink4a}$ expression was upregulated in 9.6 mJ/cm^2, yet the differences were not significant. $P16^{ink4a}$

acts as a repressor on Cyclin D2, which promotes Rbp phosphorylation and release of Rbp so that transcription becomes activated [40]. In conclusion, Cyclin D2 should be downregulated in senescent cells [40], nevertheless a study reports that upregulation of cyclin D2 has been observed in senescent keratinocytes [74]. Here, no significant downregulation of Cyclin D2 was detected in mRNA of UV-RHE.

Other genes involved in cellular stress responses are also often upregulated in senescent cells. Two key mediators of the DNA damage response, p53 and NF-kB, were tested. p53 is upstream of a DNA-damage response signal cascade. p53 promotes the entry of irreparably DNA-damaged cells into senescence or apoptosis and is regarded important for senescence induction [75][76]; although conflicting data exists. In our experiments, p53 appeared instead downregulated in 25 mJ/cm^2 UV-RHE, albeit the differences were not significant **(Fig. 10)**.

NF-kB belongs to a family of ubiquitous transcription factors that are crucial in the regulation of cell growth. NF-kB inhibits proliferation and becomes progressively activated during senescence [77]. Here, upregulation of NF-kB was not detected in UV-RHE. None of the regulational differences proved significant.

Vascular endothelial growth factor c (VEGF-C) promotes angiogenesis and inflammation *in vivo* and is upregulated by UV light in human keratinocytes [78]. VEGF-C expression was analyzed in order to test for pro-inflammatory components in the constructs, other than the secretion of pro-inflammatory cytokines. No upregulation of VEGF-C in UV-RHE was detected **(Fig. 10)**.

Matrix-metalloproteinase 1 (MMP-1) conveys degradation of extracellular matrix and is often upregulated in ageing dermis [22, 79], but also contributes to age-related changes in the epidermis, where it reduces collagen content of the basal lamina [3]. Furthermore, UV-light can trigger the expression of MMP-1 in keratinocytes, which is why its expression was addressed in this context. No significant upregulation of MMP-1 was detected in the constructs.

Taken together, the results show that an increase of senescent cells was not reflected on the level of gene expression. Despite high fluctuations, none of the observed differences proved to be significant up- or downregulation. In stress-induced senescence, however, the detection on transcriptional level is limited due to many post-translational modifications and a gene expression pattern that reliably distinguishes senescent cells from proliferative cells has not been published yet [38].

4. 2. 7 Other senescence-associated markers

Punctual condensation of chromatin (chromatin remodeling) is a DNA damage response to UV-B and other senescence stimuli. Cryosections of the constructs were stained for cell nuclei with condensed chromatin regions indicated by the histone modification γH2AX [35, 36; Chapter 4] **(Fig. 11A, right panel)**. Cell nuclei with pronounced γH2AX signals, detectable by nuclei with one to several bright red spots, were observed in 9.6, 25 mJ/cm^2 and the control construct.

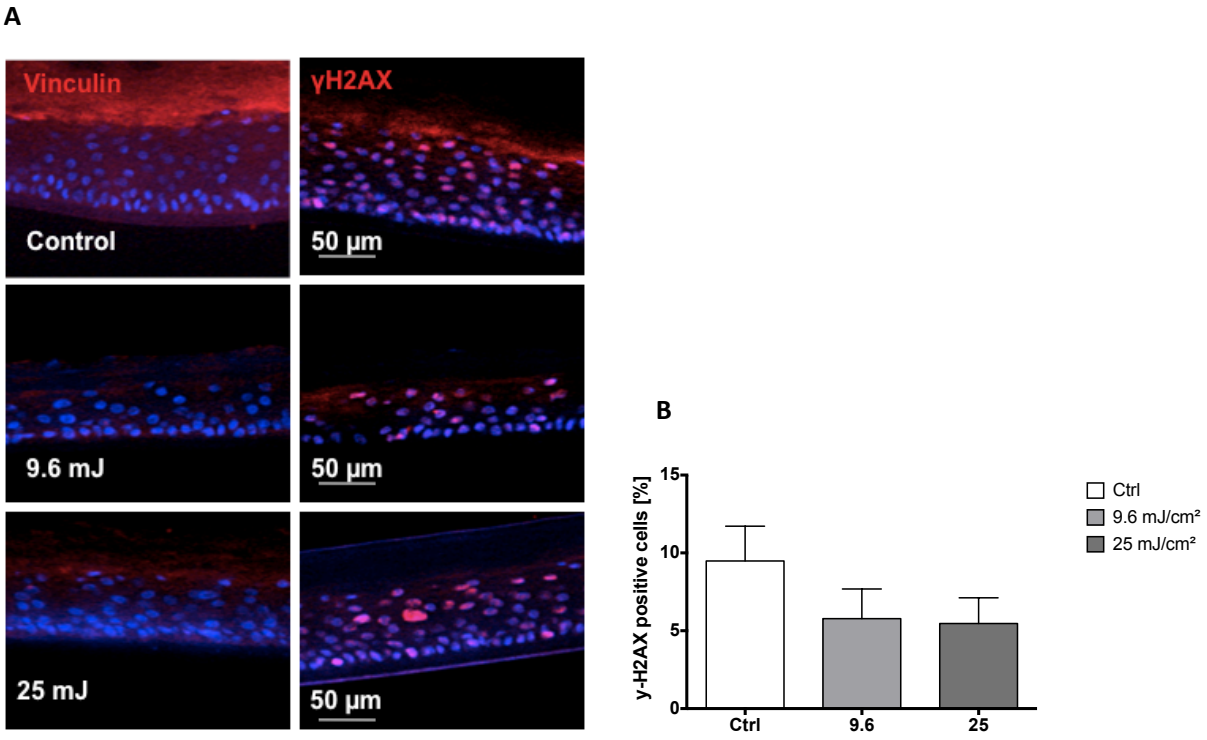

Fig. 11: A) Staining of senescence markers vinculin and γH2AX. 10 µm cryosections of the irradiated and non-irradiated constructs were immunostained with antibodies to cytoskeletal protein vinculin (red, membrane-bound) and chromosomal histone modification γH2AX (red, nuclear). Cell nuclei were stained with DAPI. Magnification: 20x. Pictures are representative of at least six donors. B) Numbers of γH2AX-positive nuclei (%), counted manually by an unbiased observer, were normalized to the total cell nuclei number. Mean ± SEM, n=6.

The normalization of γH2AX-positive nuclei to the total cell number **(Fig. 11B)** resulted in less γH2AX-positive cells in constructs from UV-irradiated keratinocytes than in the control

constructs. This means that apparently more keratinocytes with DNA damage were present in the control constructs than in 9.6 and 25 mJ/cm^2 UV-RHE.

The cytoskeletal protein vinculin **(Fig. 11A, left panel)** accumulates in focal adhesions of actin-stress fibers that are responsible for the surface increase and hypertrophy of senescent cells [80]. The formation of actin-stress fibers is related to the almost complete suppression of migratory capacity that is typical of senescent cells. Vinculin accumulation in focal adhesions has therefore been considered as marker for senescence [36; Chapter 26][81]. Positive staining of vinculin, although diffuse, was found in all constructs, but no senescence-specific localization (spot-like accumulation of vinculin in focal adhesions) could be observed. The pattern in which vinculin was expressed did not differ noticeably between 9.6 mJ/cm^2, 25 mJ/cm^2 and control construct. Like γH2AX expression, vinculin accumulation is not an exclusive marker of senescence, considering it also appears in quiescent cells. The results indicated that vinculin localization was not markedly affected here.

4. 3 Influence of UV-irradiation on percutaneous absorption

4. 3. 1 Permeation of OECD reference compounds

The OECD Test Guideline 428 defines *ex vivo* testing of percutaneous absorption. An additional document permits testing on reconstructed epidermis, given the results for a number of substances resemble those of excised skin [82]. To test the permeation in normal and UV-RHE, two model substances, the lipohilic testosterone and the hydrophilic caffeine, were chosen.

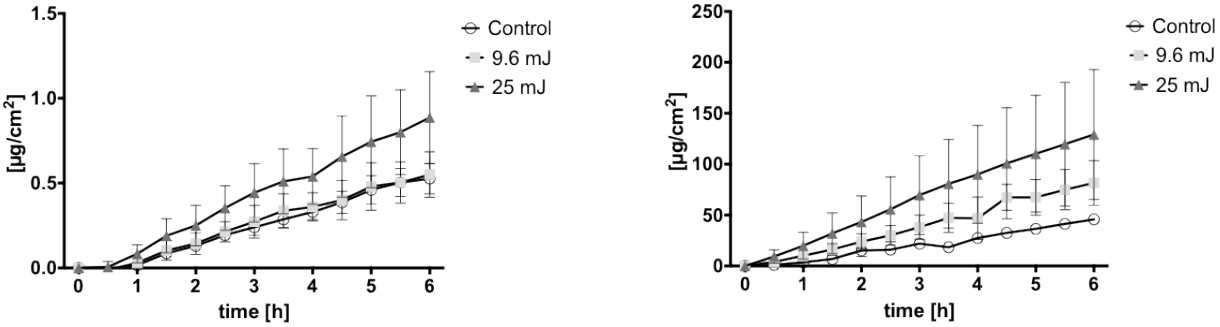

A **B**

Fig. 12: Permeability of the 25 mJ/cm² construct to testosterone (A) and caffeine (B) exceeds permeability of control and 9.6 mJ/cm² construct. Permeation was tested in cell culture inserts. 150 µl of 40 µg/ml testosterone in PBS + 0.05 % igepal and 1 mg/ml caffeine in PBS, respectively, were applied onto the constructs. Infinite-dose conditions were maintained. Cumulative amounts of radioactively labeled substance in the acceptor medium (PBS) were determined by scintillation counting. Mean ± SEM, n=3 (both substances)

RHE	Mean P_{app} value (cm/s, $x10^{-7}$) ± SEM	
	Testosterone	Caffeine
Control	6.8 ± 1.1	21.7 ± 1.7
9.6 mJ/cm²	6.9 ± 1.6	39.3 ± 9.9
25 mJ/cm²	10.7 ± 3.2	61.4 ± 30.0

The cumulative amount of permeated testosterone **(Fig. 12A)** was clearly higher in 25 mJ/cm^2 constructs than in 9.6 mJ/cm^2 and control construct. The lowest permeability was observed for the 9.6 mJ/cm^2 construct. Also, RHE provided by Prof. Brandner, UKE Hamburg-Eppendorf, was tested for permeation of testosterone. It exceeded the permeability of the UV- and control constructs after 3 h (t=3).

The permeation of caffeine **(Fig. 12B)** greatly exceeded that of testosterone **(Fig 12A)** in accordance with data on excised human skin, reconstructed full-thickness skin and epidermis. More than 10 % of the applied caffeine permeated through 25 mJ/cm^2 constructs after 6 h. The 9.6 mJ and 25 mJ/cm^2 UV-RHE were clearly more permeable to caffeine **(Fig. 12B)** than the control constructs. The P_{app}-values for caffeine of 9.6 mJ/cm^2 constructs were intermediate between control and 25 mJ/cm^2 constructs. The permeation results were very well in accordance with the reduced thickness of stratum corneum. The control constructs had lower mean P_{app} values than the commercially available epidermis model EPISKIN [14] with only 5 % permeated donor mass after 6 h. This demonstrates the overall good suitability of this type of reconstructed epidermis as test platform for permeation testing of various substances.

4. 3. 2 Penetration of Nile red loaded to CMS nanocarriers and of ICC-tagged CMS nanocarriers

The barrier function of the UV-RHE was closely investigated by the penetration of core-multishell (CMS) nanocarriers. Provided by (SFB 1112) project A01 [60], CMS nanocarriers are designed to transport drugs into viable layers of the skin without the disadvantage of systemic effects. Their penetration depth is different in healthy, diseased and tape-stripped skin and skin models [64]. Their local tolerability is exceptionally good, yet their penetration depth into skin layers, which is critical for risk assessment, has not sufficiently been investigated. In SFB project C02, CMS nanocarriers tagged with indocarbocyanine (ICC) or loaded with the drug mimic Nile red (NR) were tested on excised skin and skin models.

4. 3. 2. 1 Trace analysis indocarbocyanine (ICC)

The penetration experiments investigate the controlled penetration of nanocarriers through the stratum corneum and into the viable layers of the reconstructed epidermis. A prerequisite to this test is a fully maturated epidermis construct with closed monolayer and sufficient stratification. Leakage of the applied CMS nanocarriers tagged with ICC (indocarbocyanine) from the surface into the surrounding medium, by ways of an incomplete cell monolayer, must be excluded. Therefore, the color of the culture medium was determined by photometrical detection at 540 nm (indocarbocyanine absorbance peak at 520 nm) **(Fig. 13)**.

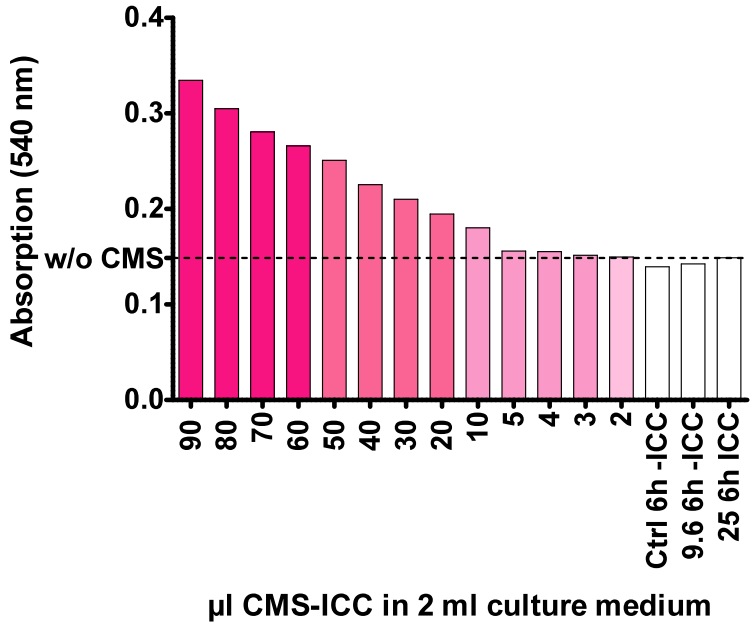

Fig. 13: After 6h incubation with 80 µl CMS-ICC nanocarriers in aqueous solution (5g/L), the color of the (surrounding) culture medium was analyzed for traces of indocarbocyanine. For reference, the color change of a dilution series of CMS-ICC nanocarriers (90-2 µl) in 2 ml medium was shown. White bars show color of medium from normal and UV-RHE penetration. Dotted line (w/o CMS) represents color of medium from mock-up experiment with 80 µl water (same batch). n=1.

It was clearly shown that the absorbance of culture medium used during CMS-ICC penetration experiments did not surmount the absorbance of medium from the parallel

mock-up experiments (with 80 µl water applied instead of nanocarriers in solution). This demonstrates that the surrounding culture medium remained free from CMS-ICC nanocarriers. It confirmed the integrity of the constructs and proves that there were no gaps between the construct and the edges of the insert. When applied to the insert membrane without any cells, CMS-ICC nanocarriers within less than 20 minutes leaked through the pores and into the surrounding medium. When applied to normal and UV-RHE cultured in inserts, this did not happen. This proved that the RHE excluded possible leakage and that cutaneous absorption can be tested on this type of RHE in a controlled fashion.

4. 3. 2. 2 Penetration of Nile red loaded to CMS nanocarriers

Nile red (NR) was used as a cargo to model a drug loaded onto the CMS nanocarriers. The penetration of Nile red loaded to CMS nanocarriers into normal and UV-RHE **(Fig. 14)** was analyzed by tracing the Nile red in the stratum corneum and the viable epidermis via conventional fluorescence microscopy. Most Nile red was detected in the stratum corneum after 3 and 6 h in all constructs. Nile red also penetrated into the viable epidermis, but the penetration was about 50% less than in the stratum corneum. No significant differences between Nile red penetration into normal and UV-RHE were detected **(Fig. 14B)**.

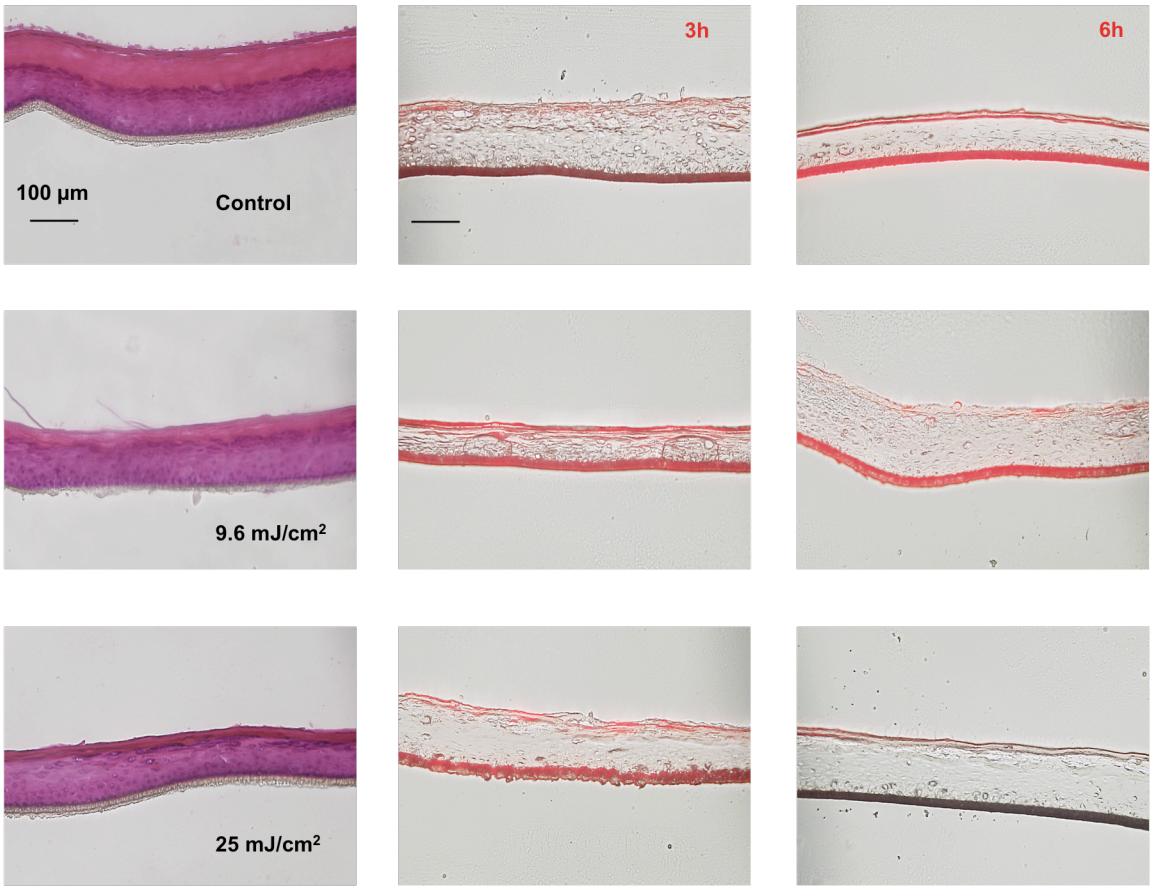

A

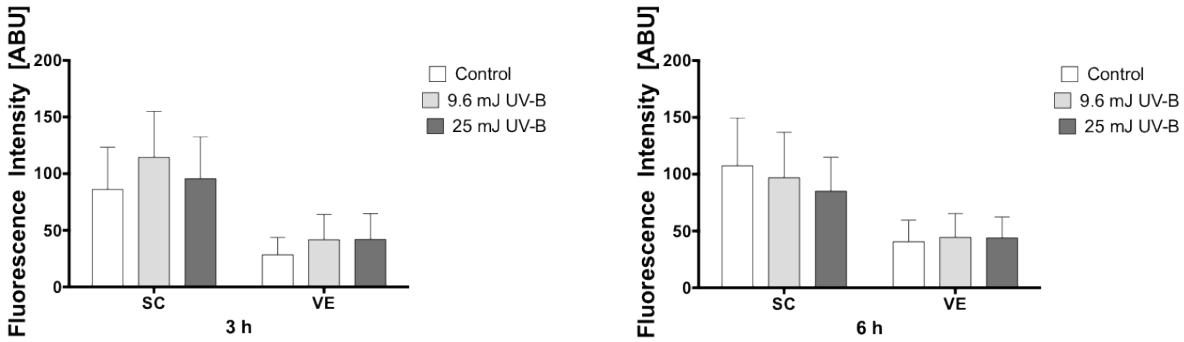

B

Fig. 14: Penetration of Nile red into reconstructed epidermis. A) 80 µl/cm^2 of CMS nanocarriers loaded with Nile red in aqueous solution (5g/L) were applied onto the constructs and kept for 3 (6) h at 37°C. 10 µm cryosections were subjected to fluorescence microscopy. Non-treated constructs of the same batch (HE staining) were used for comparison to evaluate the impact of CMS incubation on the integrity of the constructs. Magnification: 10x. Pictures are representative of at least three donors. B) Average arbitrary pixel brightness (ABU) per stratum was determined at 3 and 6 h, respectively. Mean ± SEM, n=3.

Damage of the stratum corneum, an artifact caused by swelling in the aqueous solution that contains the CMS nanocarriers and the subsequent mechanical stress of freezing and cutting into histological sections, was observed. The damage was obvious when compared to the histology **(Fig. 14A, left panel: HE-staining)** of non-treated constructs (same batch). Furthermore, auto-fluorescence of the insert membranes in varying intensity despite constant exposure times was observed. This probably resulted from uneven thickness of the sections (cryotome). Few micrometers difference in the thickness can account for different fluorescent properties. Taken together, these technical problems should be overcome and the experimental procedure should be optimized for application on epidermis constructs, which are much more susceptible to mechanic stress than full-thickness skin models.

4. 3. 2. 3 Penetration of ICC-tagged CMS nanocarriers

The penetration of not only the cargo but also the nanocarriers themselves was also tested **(Fig. 15)**. After 3 (6) h, the indocarbocyanine (ICC-) labeled CMS nanocarriers, which have the tag indocarbocyanine covalently bound to the core, were detected in the stratum corneum and only to a small degree in the viable epidermis **(Fig. 15B)**. Enhanced penetration into viable layers was found in the 25 mJ/cm^2 UV-RHE after 3 h. The stratum corneum was partially damaged, while the histology **(Fig. 15A, left panel: HE-staining)** of the respective constructs without CMS-ICC nanocarriers (same batch) was normal. This indicates that the incubation with CMS nanocarriers damaged the stratum corneum. The damage was probably due to swelling in the aqueous solution that contained the CMS-ICC nanocarriers and susceptibility to mechanical stress.

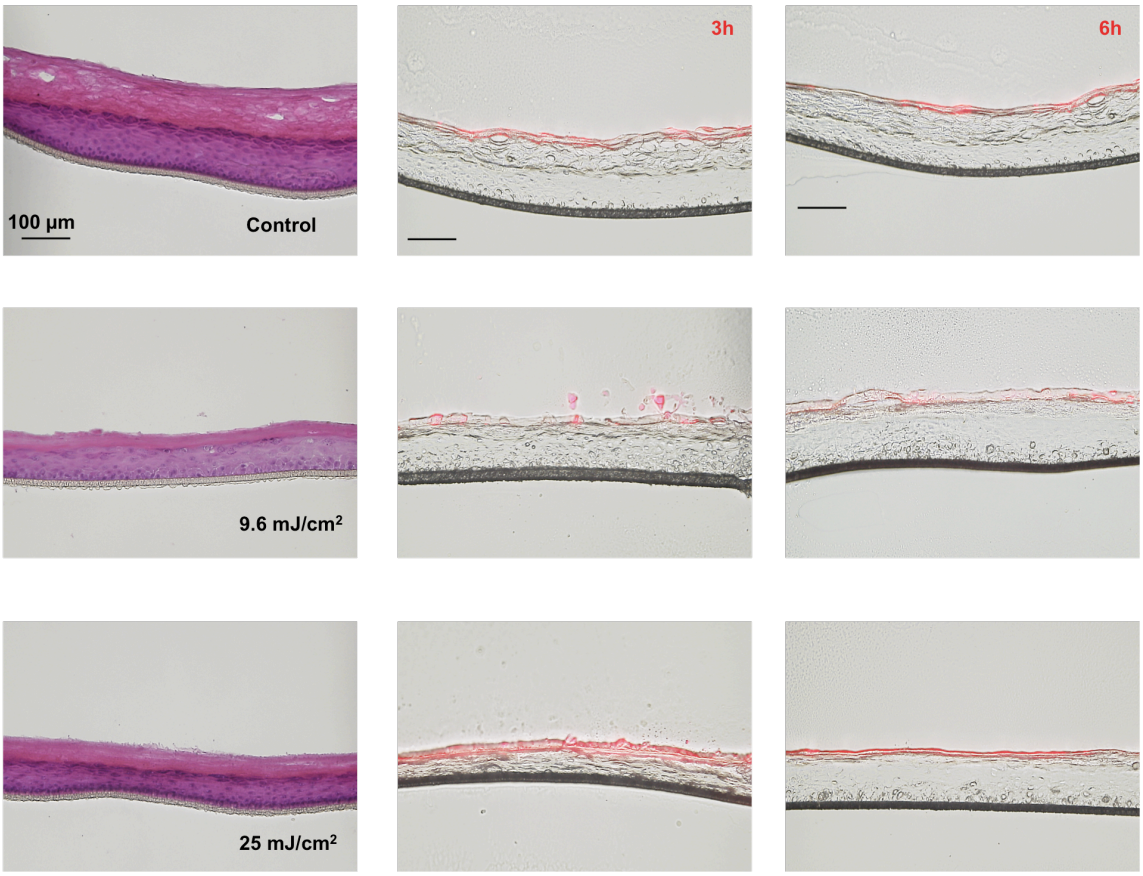

A

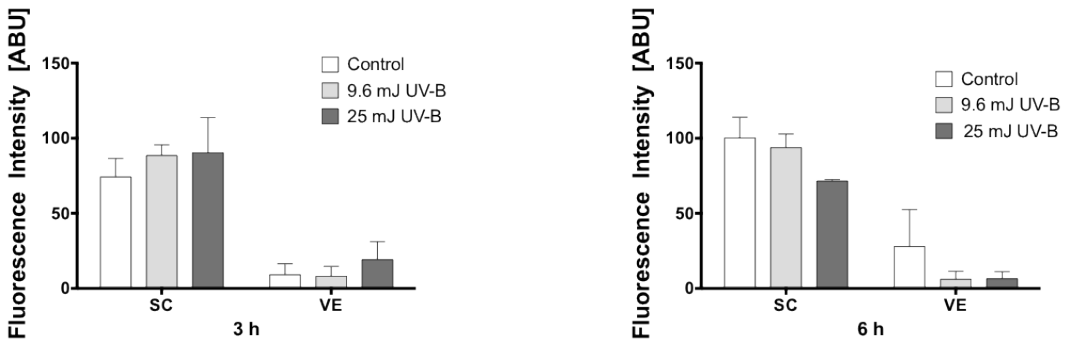

B

Fig. 15: Penetration of CMS-ICC nanocarriers into reconstructed epidermis. A) 80 µl/cm² of an aqueous CMS-ICC nanocarriers solution (5g/L) were applied onto the constructs and kept for 3 (6) h at 37°C. 10 µm cryosections were subjected to fluorescence microscopy. Non-treated constructs of the same batch (HE staining) were used for comparison. Magnification: 10x. Pictures are representative of at least three donors. B) Average arbitrary pixel brightness (ABU) per stratum was determined. Mean ± SEM, n=3.

To investigate more closely the interaction of the stratum corneum with CMS-ICC nanocarriers, the penetration over 3 and 6 h was analyzed via FLIM (Fluorescence Lifetime Imaging Microscopy) **(Fig. 16)**. FLIM was enabled in cooperation with project B03. FLIM allows for detection of CMS-ICC nanocarriers via the fluorescence lifetime of the tag indocarbocyanine and can therefore unravel possible penetration into deeper layers that are not visible in standard fluorescence microscopy.

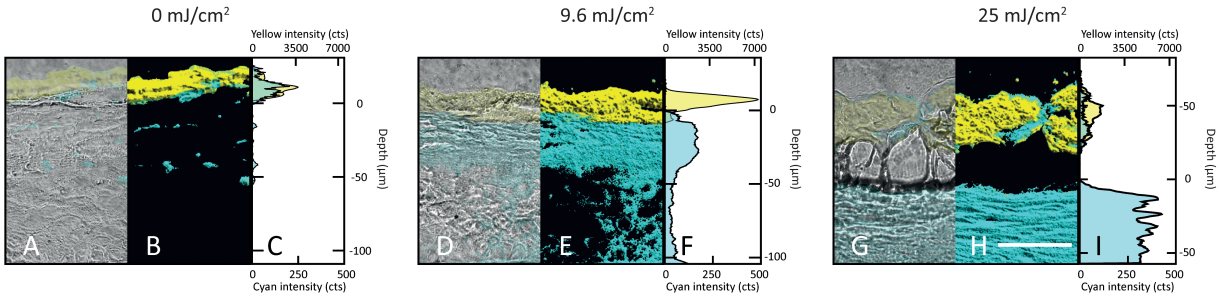

Fig. 16: FLIM analysis of 3 (6) h CMS-ICC penetration into reconstructed epidermis (9.6, 25 mJ/cm^2). 80 µl/cm^2 of an aqueous CMS-ICC nanocarriers solution (5g/L) were applied onto the constructs and kept for 3 (6) h at 37°C. 10 µm cryosections were analyzed by FLIM microscopy. Scale bar = 50 µm. Pictures represent 1 donor.

With fluorescence lifetime imaging microscopy (FLIM), the indocarbocyanine-tag of CMS nanotransporters was detected within and above the constructs. Non-penetrated leftovers of CMS nanotransporters were detected above the construct within the cryo medium (yellow in false color coding) for all three constructs, displaying a different fluorescence lifetime signature than indocarbocyanine-tagged CMS nanotransporters that penetrated the skin (blue in false color coding). Conventional fluorescence microscopy had shown that CMS-ICC nanocarriers after 6 h penetrated mainly into the stratum corneum and only to very little degree into the viable epidermis **(Fig. 15)**. FLIM revealed that CMS-ICC nanocarrier penetration into the 25 mJ/cm^2 construct was increased compared to the 9.6 mJ/cm^2 construct and the control construct **(Fig. 16)**. The increase was about twofold in the stratum corneum and about six fold with regard to the viable epidermis when comparing UV-RHE of both doses 9.6 and 25 mJ/cm^2. This demonstrates that measurement of penetration depth via fluorescence lifetime is much more sensitive than conventional fluorescence microscopy. Marginal penetration of CMS nanotransporters into the stratum corneum was found for

normal RHE. Also, the penetration after 6 h was higher than after 3 h. All in all, increased penetration up to 10-fold higher was found in the 25 mJ/cm^2 UV-RHE after 6 h compared to the normal RHE after 3 h. It is concluded that the CMS-ICC nanocarrier penetration depth rises with UV-B irradiation dose and time.

5 Discussion

5. 1 UV-B induced senescence in keratinocyte monolayers

The increase of senescence-associated ß-galactosidase by 1.5 fold at 25 mJ/cm^2 UV-B **(Fig. 1B)** in relation to the non-irradiated control confirmed an UV-induced effect on the cells. Since the keratinocytes had been isolated from juvenile foreskin, the increase in senescent cells occurred independent from the cell age and was therefore induced prematurely through UV irradiation. Thus, a type of premature or stress-induced senescence was inducible. Also at 9.6 mJ/cm^2 UV-B, a moderate increase (1.25 fold) in ß-galactosidase-positive keratinocytes was detected **(Fig. 1B)**. This was particularly interesting considering that several publications reported that UV doses in this range were not powerful enough to induce effects in keratinocytes. Again, direct comparison of reported UV-B doses was rendered difficult by the use of different UV sources. However, Lewis et al. [39] showed an increase in senescent keratinocytes at 10 mJ/cm^2 UV-B. Here, in agreement with Lewis et al., we found an at least moderate increase in senescent cells at 9.6 mJ/cm^2. While considered the most reliable (or only) marker of senescent cells to date, even the expression of SA-ß-galactosidase is not 100 % exclusive, considering it can sometimes occur in highly confluent cells [45]. Therefore, importantly, the senescent phenotype was not only confirmed by SA-ß-galactosidase expression but also by the cell morphology **(Fig. 1A).** The morphological changes were typical of senescence [42] with hallmark features such as flattening, size increase, and enlarged nuclei. Together with the fold increase of SA-ß-gal-positive cells **(Fig. 1B)**, this observation proved that the experimental setup chosen here was successful to trigger premature senescence in keratinocytes.

5. 2 UV-B effect on viability and proliferation

The viability after UV irradiation in monolayers keratinocytes declined in a time-delayed manner by up to 30% after 72 h at 25 mJ/cm^2 UV-B **(Fig. 2)** and was already reduced by 25% after 24 h. If the same applied to UV-RHE, critically damaged cells were presumably cleared from the culture. Regarding the effect of UV irradiation on the proliferation of keratinocytes,

there has been much controversy. Reduced, but also increased proliferation was reported [19, 83]. Reduction of proliferation by 70 % had been observed. Also at comparably low doses (12.5 mJ/cm^2), reduction by 20 % was detected [19]. Here, keratinocytes treated with 9.6 mJ/cm^2 were not affected, but those treated with 25 mJ/cm^2 were reduced in their proliferation by 25 % **(Fig. 3)**. If applied to the cultured UV-RHE, this could have had an impact, as fewer proliferative keratinocytes in the basal membrane lead to slower tissue turnover and slower differentiation [68].

5. 3 Morphology of UV-RHE

Regarding the effect of UV light on differentiation in keratinocytes, conflicting data had been reported: differentiation was mostly disturbed, but, probably depending on the UV dose, in some other cases stimulated by the irradiation [84]. Here, although 25 mJ/cm^2 UV-RHE stained positive for markers of early and late differentiation, some other features indicated abnormalities in the differentiation process, such as the irregular pattern of keratinocytes in the basal lamina and the stratum spinosum **(Fig. 5: d, e)**. Interestingly, the phenotype of 9.6 mJ/cm^2 UV-RHE shared in part features of both 25 mJ/cm^2 UV-RHE and normal RHE, which indicated a dose-dependency on the degree of differentiation disturbance. Also, the hyperchromatic stratum granulosum and signs of acantholysis in 25 mJ/cm^2 UV-RHE pointed to disturbed differentiation in accordance with aged human epidermis *in vivo*, that often lacks homeostasis of keratinocytes undergoing proliferation, differentiation and desquamation. This disturbance is often accompanied by the lack of an appropriate calcium gradient from the basal to the top layers [3, 6].

The observed effects must be discriminated from other UV-B effects on skin, which are commonly discussed in this context but are mostly associated with thickening of the epidermis (known as “photoageing”). The signs of photoageing (e.g. thicker stratum corneum, loss of elasticity) occur after repeated doses of UV-B irradiation and develop over years [86, 87]. In this study, the keratinocytes were treated with single-dose UV-B exclusively and grown over a period of 14 days. Therefore photoageing is not regarded as relevant to explain the morphology observed in constructs from UV-B irradiated keratinocytes.

5. 3. 1 Thickness of stratum corneum and viable epidermis

The stratum corneum of the 25 mJ/cm^2 UV-RHE was reduced by over 50 % compared to the normal RHE **(Fig. 6B)**. The stratum corneum of the 9.6 mJ/cm^2 UV-RHE was reduced by about 30 %. Also the thickness of the viable epidermis was reduced by about 10 %. It was tested whether fluctuations in the seeding numbers influenced the morphology **(Fig. 6A)**. The reduction of the cell number by 50 % of the standard number **(Fig. 6A, upper panel)** resulted in unchanged amounts of stratum corneum and viable epidermis. This indicated that the reduced stratum corneum was not caused by fluctuations in the seeding numbers. Thus, the reduced thickness was caused by the UV irradiation. Since the total keratinocyte count was not markedly different in 25 mJ/cm^2 UV-RHE, thinner layers resulted from flattened keratinocytes and/or exfoliated corneocytes. This fits in with data on the thinning of aged human epidermis, where a thinner stratum corneum and fewer viable layers occur during ageing *in vivo* [68, 85].

The morphology was in agreement with the proliferation reduction at 25 mJ/cm^2 UV-B in monolayer keratinocytes **(Fig. 3)**. Since senescent cells do not incorporate BrdU, they were reflected in the number of non-proliferative cells. Fewer proliferative keratinocytes in the basal lamina lead to slower tissue turnover and slower differentiation and generation of the stratum corneum [68], which applies to aged epidermis *in vivo* [6]. A role for senescence in the morphological changes is in accordance with other publications, where a glycated dermis equivalent [17] or the prolonged cell culture [18] also caused thinning of the epidermis. Here, in accordance with the increased ß-galactosidase expression **(Fig. 8),** it is suggested that keratinocytes underwent UV-B induced senescence (which occurs up to 72 h following the stimulus) and influenced stratification of the different stratae by their structure and inflammatory secretion, altering cell-cell communication [24]. With regard to the reduced viability at 25 mJ/cm^2, it can be assumed that critically UV-damaged keratinocytes were cleared from the culture altogether. It was reasonable to argue that keratinocytes seeded into inserts were affected similarly to the monolayer cultures because they were irradiated with the same UV-B doses following the same protocol.

5. 3. 2 Tight-junction proteins

The existence of an appropriate barrier function is an important factor in reconstructed skin, and tight junctions play an important role for the physiological skin barrier *in vivo*. Not only the lipids of the stratum corneum, but also the tight-junctions underneath are important for appropriate barrier function. They seal the spaces between neighboring cells and form a tight barrier, which can be regulated in a dynamic manner in response to the environment [49]. Here, the tight-junction protein claudin-1 was expressed in all constructs (9.6, 25 mJ/cm^2 UV-RHE and control) **(Fig. 7)**, which indicated the existence of a functional barrier. This accentuated the general high quality of the RHE. Previously, a study had reported disturbance of TJ protein expression in human keratinocytes following UV-B irradiation **[48]**. With the data presented here, this effect was not confirmed. Contrarily to the disturbed cell nuclei pattern in DAPI-stained UV-RHE **(Fig. 5: d)**, the expression of tight-junction protein claudin-1 was normal. Consequently, the reduced thickness of the stratum corneum was probably more important for the increased permeation and penetration observed in 25 mJ/cm^2 UV-RHE.

5. 4 Expression of ß-galactosidase in UV-RHE

The expression of senescence-associated ß-galactosidase (SA-ß-Gal) at pH 6 also correlates with increased total protein levels of ß-galactosidase [44, 88]. ß-galactosidase expression was detectable in tissue lysates from 25 mJ/cm^2 UV-RHE **(Fig. 8)**. It was absent in 9.6 mJ/cm^2 UV-RHE and normal RHE, which was attributed to the detection limit of the Western Blot that captured the relative increase. Together with the results from monolayer cultures of UV-B irradiated keratinocytes **(Fig. 1)**, this was indicative of the existence of senescent cells in the 25 mJ/cm^2 UV-RHE. This nicely paralleled an important feature of aged tissue *in vivo* [89, 90]. It is known that abundance of senescent cells alter the tissue structure and function and foster age-related changes [8]. Here, the senescent keratinocytes presumably contributed to the altered morphology of UV-RHE. Importantly, with the method here it was possible to detect ß-galactosidase expression in lysates from RHE tissue and in accordance with the UV-stress. Most publications on keratinocyte senescence investigated the

expression in monolayers. Despite the published protocols [45], the in-situ detection of ß-galactosidase is reportedly difficult [97] and was not feasible in other approaches to mimic ageing [17].

5. 5 Secretion of cytokines

It is long known that senescent cells secrete increased levels of a set of pro-inflammatory cytokines (SASP), including IL-1α and IL-8 [92]. The SASP cytokines presumably exert paracrine effects on other cells in the surrounding tissue [24]. The culture medium was tested for the pro-inflammatory cytokines IL-1α and IL-8 **(Fig. 9)**, which are part of the secretome of senescent cells, but are also induced in response to UV-B irradiation. Pro-inflammatory cytokines such as IL-8 are secreted as an acute reaction to UV-B light *in vivo* and *in vitro* [91], but generally reach a maximum 24-48 h post-stimulus [83]. Elevated levels of IL-8 were detected in 25 mJ/cm^2 UV-RHE 14 days post-stimulus **(Fig. 9B)**. Therefore, the high IL-8 level detected at day 14 of the culture cannot be viewed as an acute effect, but rather represents a long-term consequence of the irradiation. The time-delayed, increased IL-8 secretion was therefore likely caused by a build-up of an inflammatory environment in the UV-RHE through the presence of senescent cells. This nicely paralleled the chronic, low-level inflammation of aged tissues *in vivo* [24]. IL-1α **(Fig. 9A)**, another pro-inflammatory cytokine of the SASP, reacts to DNA damage as the master of the secretion cascade. It leads to the expression of IL-8 as a downstream effector and fittingly preceded IL-8 expression over the course of the cultivation. The comparably low amounts of IL-1α in the medium were attributed to a fast degradation. Previous studies have shown that IL-1α is difficult to quantify in culture medium due to its susceptibility to degradation by added components.

5. 6 Gene expression

On transcriptional levels, a defined regulation pattern for senescence has not been described yet. To date, several studies have focused on the up- or downregulation of genes that are related to cell cycle progression or –inhibition, such as p16^{INK4a} and cyclin D2 in senescent human keratinocytes [72, 93]. These are genes associated with the proliferation arrest that is irreversible in senescent cells. Additionally, regulators of the DNA damage

response that precedes senescence, such as the transcription factor NFkB, were tested. In theory, NFkB should be upregulated in parallel to IL-1α secretion [37] **(Fig. 9A)**, which was not detected here. With the data presented here **(Fig. 10)**, no significant upregulation of senescence-associated genes was observed. Likewise, no differences were detected in the mRNA of several functional proteins related to the architectural changes of the epidermis during ageing (collagen 7, MMP-1) or indicative of inflammation (VEGF-C). It should be accentuated that senescence not always reflects on the mRNA because of posttranslational modifications [38, 73]. Therefore, detection of senescent cells by their gene expression is very limited. Also, the choice of an appropriate housekeeping gene is challenging when a potent stimulus like UV light is involved. Here, GAPDH (glyceraldehyde 3-phosphate dehydrogenase) was chosen because supportive data stated that GAPDH has no apparent UV-B related regulation [52]. However, in a different study, it was suggested that GAPDH gene expression in the epidermis was actually highly increased by UV-B [94]. If the latter applied to our experiment, it could explain why upregulation of senescence-associated genes was not detectable. A thorough evaluation of housekeeping genes that are better suited for an experiment involving UV irradiation, or yet a combination of different housekeeping genes, would be useful to help clarify this issue.

5. 7 Other senescence-associated markers

H2AX, part of the histone H2A family, is a senescence-associated marker that is phosphorylated and forms foci at DNA strand break sites in response to DNA damaging incidents [35, 40]. Here, normalization of γH2AX-positive keratinocytes to the cell number **(Fig. 11B)** indicated more DNA-damaged cells in normal RHE than UV-RHE. Although DNA damage precedes senescence, the formation of heterochromatin foci is not indispensable for senescence. It should be stressed that the importance of γH2AX as a senescence marker is under debate as it may occur independently from senescence [95, 96] (reviewed in [40]). This makes γH2AX a non-specific senescence marker, while ß-galactosidase overexpression **(Fig 1, Fig. 8)** is much more specific [42]. Moreover, the formation of γH2AX foci is closely associated with upregulation of $p16^{INK4a}$, suggesting that a functional interaction between the two exists. Bearing this correlation in mind, unchanged mRNA levels of $p16^{INK4a}$ in UV-RHE **(Fig. 10)** are in accordance with the missed expectation of increased numbers of γH2AX-

positive cells. Yet, neither $p16^{INK4a}$ overexpression nor γH2AX heterochromatin foci seem ultimately required for senescence, as there is evidence that proliferative arrest can circumvent $p16^{INK4a}$ expression, and besides, γH2AX foci might only be inducible under certain conditions (e.g. specific types of oncogene-induced senescence; reviewed in [40]). Thus, in the broader picture, the higher proportion of γH2AX-positive keratinocytes in control constructs **(Fig. 11B)** does not necessarily contradict the assumption that more senescent keratinocytes are present in UV-RHE, as detected in the Western Blot **(Fig. 8)** or indicated by monolayer ß-galactosidase expression **(Fig. 1)**.

Another senescence-associated marker, the cytoskeletal protein vinculin **(Fig. 11A, left panel),** displays spot-like accumulations in focal adhesions of actin-stress fibers that are responsible for the flattening of senescent cells [80]. Flattening of ß-galactosidase-positive senescent keratinocytes had been appropriately detected in the monolayer **(Fig. 1A)**, but was not reflected in vinculin localization in the UV-RHE, where vinculin staining was diffuse. Senescence-typical vinculin accumulation had been successfully detected in monolayers before [80], yet it was not established as a marker for the detection of senescent cells in tissue sections. Thus, in like manner as it is reportedly difficult to detect ß-galactosidase in situ via the conventional colorimetric assay [17, 97], distinct vinculin staining might have been missed out in the complex structure of the tissue sections in contrast to monolayers.

5. 8 Influence of UV-B irradiation on percutaneous absorption

5. 8. 1 Permeation of OECD reference compounds

Permeation testing in plastic inserts was established here on normal and UV-RHE. Netzlaff et al. [99] had evaluated this method and found no significant differences to the testing in Franz cells that was used in the ATLA study [98]. Therefore, the results could be directly compared. To test the predictive power of the normal and UV-RHE according to the procedures of the validation study for RHE [98], two OECD reference compounds were used. The permeation of caffeine **(Fig. 12B)** largely exceeded that of testosterone **(Fig. 12A)** in all constructs. This was in agreement with studies on reconstructed epidermis as well as excised

human and porcine skin *ex vivo* and corresponded to the more hydrophilic nature of caffeine [14]. The stratum corneum is the layer that has the largest influence on the permeation. In accordance with the thin (25 mJ/cm^2 UV-RHE) and intermediate (9.6 mJ/cm^2) stratum corneum **(Fig. 6)**, caffeine and testosterone permeation was clearly highest in the 25 mJ/cm^2 UV-RHE and thereby fitted in with data on aged skin *in vivo*, where the permeability was increased due to the structural changes in the stratum corneum [9]. In the case of caffeine, the permeation of 9.6 mJ/cm^2 constructs exceeded that of the control constructs, reflecting a reduction of stratum corneum thickness intermediate between normal and 25 mJ/cm^2 UV-RHE, yet the differences were more obvious in the 25 mJ/cm^2 constructs.

Regarding testosterone permeation, the differences between batches were comparably high and increased with UV dose. They were up to 10-fold in UV-RHE (25 mJ/cm^2) compared to two-fold in the respective control construct. This is in accordance with previous studies where tremendous inter-individual differences in the elderly in terms of skin structure and function were reported [100]. Nevertheless, in accordance with the decreased cohesiveness and altered lipids of the stratum corneum in the elderly [9, 53], a clear trend could be detected towards an impaired barrier function in 25 mJ/cm^2 UV-RHE. If additional data will be able to confirm this trend in the future, the higher permeability should be considered in the development of skin drugs. Tailor-made treatments that take into account the differences would be beneficial to a growing number of elderly patients. Still, the permeability of aged skin remains subject of ongoing research, as data from some *in vivo* studies even point to the opposing trend of rather decreased permeability [101].

Typically, appropriate barrier function that is comparable to human skin is an issue in many commercially available skin constructs. Despite the great resemblance of human skin *ex vivo* to reconstructed skin, reconstructed skin has a different lipid composition with comparably higher amounts of triglycerides and lower amounts of polar ceramides (reviewed in [13]). As a result, the barrier function of reconstructed skin is often lower than that of excised human skin. In this study, the P_{app}-values of the normal RHE indicated that this type of reconstructed epidermis had a stronger barrier function than commercially available epidermis models (P_{app} EPISKIN testosterone: 2.10 cm/s x 10^{-6}; caffeine: 2.94 cm/s x 10^{-6})[98]. Together with the appropriate ratio of caffeine versus testosterone permeation, the reconstructed

epidermis that was developed here is a suitable test platform for the permeation of lipophilic and hydrophilic drugs.

5. 8. 2 Penetration of Nile red loaded to CMS nanocarriers

The penetration of the drug-mimic Nile red was analyzed with conventional fluorescence microscopy **(Fig. 14)**. Previous studies had shown clearly increased penetration of Nile red into barrier-deficient skin [64] and barrier-impaired reconstructed skin [59]. Namely by tape-stripping of the stratum corneum, a facilitation of penetration with barrier impairment had been detected, albeit a definite correlation of the stratum corneum thickness with penetration depth was not confirmed [64]. Here, despite a thinner stratum corneum in 25mJ/cm^2 constructs and indications to weaker barrier function (as demonstrated by the permeation of OECD reference compounds), no clear trend was observed regarding penetration depths of Nile red into normal and UV-RHE. All in all, the nanocarrier served its purpose to transport the drug mimic Nile red into viable layers of the RHE, but the previous data that demonstrated faster penetration on decreased barriers [64] was not entirely confirmed. To test if CMS nanocarriers truly enhance the penetration of the Nile red, a dye-only control of the Nile red would be needed, which is not available to date due to the insufficient solubility of mere Nile red in water and the side effects of possible solvents like ethanol. Also, likewise the analysis of the CMS-ICC penetration, disruption of the tissue by mechanical stress was an issue for the accuracy of the penetration depth measurement that should be overcome in the future.

5. 8. 3 Penetration of ICC-tagged CMS nanocarriers

Conventional fluorescence microscopy detected penetration of CMS-ICC nanocarriers into the stratum corneum in all constructs and only to very little degree into the viable epidermis **(Fig. 15A,B)**. The far more accurate FLIM analysis **(Fig. 16)** revealed that CMS-ICC nanocarriers penetrated depending on UV-B dose and time. Using this highly sensitive method, even penetration into the viable layers was detectable. The increase was about twofold in the stratum corneum and about six fold with regard to the viable epidermis when comparing UV-RHE from both doses 9.6 and 25 mJ/cm^2. In accordance with previous results

[64], the penetration was time-dependent, being higher after 6 h than after 3 h. The differences in the penetration strength indicated a compromised barrier function in 25 mJ/cm^2 UV-RHE. Increased penetration of CMS-ICC nanocarriers had been observed for barrier-deficient skin and RHE mimicking skin diseases that bring about barrier deficiency [64]. The penetration of CMS nanocarriers had never been tested on aged skin specifically, but this was important with regard to reduced barrier function observed in aged skin *in vivo* [9, 53]. The results are important for the risk assessment of core-multishell nanocarriers, given the similarity of the 25 mJ/cm^2 UV-RHE to the properties of aged epidermis *in vivo.* Because efficient skin care and drugs for the treatment of skin diseases are needed for a growing population of elderly people, drug delivery systems must take into account the age-related changes in the penetrability. To this purpose, 25 mJ/cm^2 UV-RHE could serve as a useful test platform, because a clear trend towards higher uptake in UV-RHE compared to the normal RHE was detected.

Partial disruption and damage of the stratum corneum was observed in several of the constructs after 3 and 6 h **(Fig. 15A, left panel: HE-staining)**. Due to the aqueous solution that contained the CMS nanocarriers, the reconstructed epidermis swells and becomes more susceptible to mechanical stress (freezing in liquid nitrogen, cutting of histological sections). The damage of the construct surface poses a problem for the accuracy of penetration studies. Therefore, the protocol needs to be optimized for reconstructed epidermis, which is more susceptible than excised skin or reconstructed full-thickness skin.

5. 9 Conclusion and future prospects

A new type of reconstructed epidermis was established that included UV-B irradiated prematurely senescent human keratinocytes. The constructs were tested for similarities (histology, senescence markers, permeation and penetration) to aged epidermis *in vivo* characterized by the abundance of senescent cells. 25 mJ/cm^2 UV-RHE had the most strikingly different phenotype. The resemblance to aged epidermis was given in terms of morphology, increased IL-8 secretion, senescence-associated ß-galactosidase expression and increased permeation and penetration.

Previous approaches to mimic aged epidermis or full-thickness skin have tremendously advanced the field. Nevertheless, they have also encountered problems. For example, premature induction of senescence in fibroblasts by application of a drug, mitomycin, [16] represents a similar approach to the one described here, in the way that cells were induced to premature senescence by a stimulus. Still, mitomycin is a powerful drug that might have unwanted effects on the cells and is less physiological than UV irradiation. A different approach towards a reconstructed full-thickness skin by Pennacchi et al. [17] used a glycated dermal compartment to mimic the glycosylation observed in aged skin. Their approach was devoid of an aggressive stimulus to induce ageing, but at the same time only focused on one symptomatic aspect of aged skin.

UV irradiation, in the contrary, has many advantages as it is a more physiological stimulus and also cheap and easy to apply. Also, UV-B induced effects of photodamage in skin overlap with those of chronologically aged skin [102-104], for example in terms of transepidermal water loss and the degradation of collagens by activity of matrix-metalloproteinases. Taking the overlap with chronological ageing into account, several other publications describe UV irradiation after maturation of the barrier function 7 or 14 days into the cultivation of RHS [105], RHE [47] or skin xenografts [102]. They observed effects with many similarities to aged skin *ex vivo*, yet senescence-associated ß-galactosidase staining in the tissue, to date the only reliable marker of senescence, was barely feasible.

In contrast, UV-irradiation of the keratinocytes before seeding, as described in this thesis, allowed for cultivation and testing for ß-galactosidase in keratinocyte monolayers parallel to the UV-RHE, which made it possible to test for the dose-dependent increase in senescence. This made the UV-irradiation before the seeding an innovative and interesting approach. However, the disadvantage of this method was the insufficient separation of UV-induced senescence from other UV-induced effects. Also, being a potent inducer of inflammation, UV-B irradiation stimulates immune reactions as during acute erythema [83]. Here, despite increased secretion of proinflammatory cytokines, indicators to an activated immune response had not been specifically screened for. To circumvent UV-specific effects, senescence could be induced in juvenile keratinocytes via a different stressor. Insufficient oxygen supply has been shown to prematurely induce senescence in cells through hypoxia

signaling [106]. If technically feasible (e.g. cultivation of keratinocytes under oxygen starvation in a pressurized chamber), the keratinocytes would be used for the reconstruction of RHE and exert senescence-specific characteristics omitting the overlap with UV effects.

Prospects for the future to optimize our in-house reconstruction of aged skin focus on the use of aged fibroblasts from donors at least 50-60 years old for reconstructed full-thickness skin. These experiments are underway, and with regard to the keratinocyte-fibroblast crosstalk [71], they have already given promising results that aged fibroblasts also lead to a thinner epidermis as in aged skin *in vivo* (C. Hausmann, unpublished observation). The development of reconstructed aged full-thickness skin would mimic age-related changes of both the epidermis and the dermis and therefore include more aspects. Yet, UV-RHE is comparably cheaper and less time-consuming than the cultivation of RHS and able to represent several important key aspects of aged skin on a laboratory scale.

Summary

Reconstructed full-thickness skin (RHS) and reconstructed epidermis (RHE) has proven a promising alternative to preclinical drug testing on animal (pig, mouse) skin, which should be overcome both due to ethical concerns and species-related differences that question the predictive power. Constructed from juvenile cells, the available models omit changes that occur in the skin during ageing. Reconstructed epidermis that can mimic age-related changes is particularly relevant with regard to the growing population of elderly people. Previous approaches to meet this need included the use of a glycated dermis equivalent to reflect age-related glycosylation, or fibroblasts prematurely aged by replicative senescence through prolonged cultivation or drug-induced senescence by mitomycin treatment. Here, it was intended to induce senescence in juvenile keratinocytes by UV-light and to construct UV-RHE. Single doses of UV-B (25 mJ/cm^2) are sufficient to cause senescence in keratinocytes, as indicated by expression of senescence-associated (SA)-ß-galactosidase and characteristic morphology (flattening, size increase and strong granulation). Keratinocytes irradiated with 25 mJ/cm^2 UV-B and one lower dose, 9.6 mJ/cm^2, and non-irradiated control keratinocytes, respectively, were seeded into inserts and cultivated for 14 days to form normal RHE and UV-RHE. In parallel, the effect of the UV irradiation on cell viability and proliferation was investigated in keratinocyte monolayers. It was found that 25 mJ/cm^2 UV-B reduced the viability to about 30 % 72 h post-irradiation. The cell proliferation decreased by about 25 % at the same dose after 72 h. Moderate effects were detected for the lower dose. The normal and UV-RHE were investigated after 14 days. The normal RHE displayed the appropriate regular pattern of erect keratinocytes in the basal lamina and was fully stratified, while the UV-RHE showed an irregular pattern, indicating disturbed differentiation. The most obvious distinction was a dose-dependent reduction in the epidermal layers: in 25 mJ/cm^2 UV-RHE, the stratum corneum shrunk by 56 % ($p \leq 0.01$) and in 9.6 mJ/cm^2 UV-RHE by about 30 %. The thickness of the viable epidermis was also reduced, although less remarkably. Since the effects were demonstrably not caused by fluctuations in the seeding numbers and the keratinocyte count in normal and UV-RHE was not markedly changed, the reduction presumably resulted from flattened keratinocytes and/or exfoliated corneocytes. The thinning of the epidermal layers nicely paralleled the epidermal atrophy *in vivo*, where

senescent cells cause structural and functional alterations of the tissue. In order to test the influence of the UV stress on the secretion of pro-inflammatory cytokines, IL-1α, IL-6, IL-8, IL-12, and TNFα were tested. Only IL-1α and IL-8 were above the detection limit and were elevated in 25 mJ/cm^2 UV-RHE throughout the cultivation by about twofold compared to normal RHE. IL-1α levels were highest at day 2 and preceded elevated IL-8 levels from day 7 to 14. Elevated IL-1α and IL-8 levels are part of the senescence-associated secretory phenotype (SASP) that is characteristic of the chronic inflammation of aged tissues. Increased ß-galactosidase protein levels in tissue lysates were at least detectable for two batches of 25 mJ/cm^2 UV-RHE. Together with the monolayer results of increased ß-galactosidase expression and the elevated IL-1α and IL-8 levels, the existence of senescent cells in UV-RHE in accordance with ageing tissues *in vivo* is strongly suggested. To investigate the barrier function of normal and UV-RHE, the permeation of two OECD reference compounds was tested. Caffeine and testosterone both permeated UV-RHE faster than normal RHE, and despite relatively strong inter-batch differences clearly pointed to barrier impairment in 25 mJ/cm^2 UV-RHE in agreement with structural and functional alterations of the stratum corneum in the elderly. Also, the uptake of core-multishell (CMS-) nanocarriers was tested. CMS nanocarriers are promising as efficient drug transporters for the treatment of skin diseases; yet their penetration into aged skin with altered barrier function, critical for their risk assessment, had not been investigated. In accordance with the decreased barrier of 25 mJ/cm^2 UV-RHE, an increased penetration of indocarbocyanine-tagged nanocarriers by comparison to normal RHE of about twofold into the stratum corneum and about six fold into the viable epidermis was detectable via FLIM (fluorescence lifetime imaging microscopy). Taken together, a new type of reconstructed epidermis was built from UV-B stressed keratinocytes that was able to capture the most evident hallmarks of skin ageing *in vivo.* The resemblance to aged human epidermis was given in terms of morphology, increased IL-1α and IL-8 secretion, senescence-associated ß-galactosidase expression and increased permeation and penetration.

Zusammenfassung

Rekonstruierte humane Vollhaut- (RHS) und Epidermismodelle (RHE) für die präklinische Testung sind eine vielversprechende Alternative zu den ethisch bedenklichen Tierversuchen. Ihr entscheidender Vorteil ist, dass sie, anders als Schweine- oder Maushaut, aus menschlichen Zellen aufgebaut werden und damit das Problem artspezifischer Unterschiede umgehen. Da RHS und RHE stets aus juvenilen Spenderzellen generiert werden, sind die strukturellen und funktionalen Unterschiede, wie sie in gealterter Haut auftreten, in diesen Modellen bisher nicht ausreichend berücksichtigt. Aufgrund eines zunehmenden Bevölkerungsanteils älterer Menschen ist die entsprechende Anpassung ein wichtiges Ziel. Bisherige Ansätze zur Modellierung von Hautalterung beinhalteten unter anderem die Verwendung eines gykosylierten Dermisäquivalents sowie die Induktion von Seneszenz durch verlängerte Kultivierdauer oder Gabe von Mitomycin. Der hier gewählte Ansatz beschreibt die Induktion von Seneszenz in juvenilen Keratinozyten durch UV-Stress. Einmalige Bestrahlung mit UV-B (25 mJ/cm^2) kann Seneszenz in juvenilen Keratinozyten hervorrufen, wie durch 1.5 fache Erhöhung seneszenz-assoziierter ß-Galaktosidaseexpression und charakteristischer Veränderungen der Zellmorphologie (Abflachung, Oberflächenvergrößerung und starke Granulierung des Zytoplasmas) gezeigt. Mit zwei verschiedenen UV-Dosen (25 mJ/cm^2; 9.6 mJ/cm^2) bestrahlte Zellen, sowie die Zellen der unbestrahlten Kontrolle wurden über 14 Tage zu normaler bzw. UV-RHE kultiviert. Der Effekt der UV-Strahlung auf Viabilität und Proliferation wurde am Monolayer untersucht, mit bis zu 30 % verringerter Viabilität und 25 % verringerter Proliferation bei 25 mJ/cm^2 UV-B 72 h nach der Bestrahlung. Nach dem Ende der 14-tägigen Kultivierung in Inserts zeigte die normale RHE die angemessene Ausbildung aller epidermalen Schichten sowie die typische, aufrechte Anordnung der Keratinozyten in der Basalmembran. Die UV-RHE dagegen hatte eine unregelmäßige, auf eine gestörte Differenzierung hinweisende Anordnung der basalen Keratinozyten. Am auffälligsten war jedoch der dosisabhängige Dickenunterschied der epidermalen Schichten. 25 mJ/cm^2 UV-RHE hatte ein um durchschnittlich 56 % ($p \leq 0.01$) verringertes Stratum corneum (circa 30 % in 9.6 mJ/cm^2 UV-RHE). Die Dicke der viablen Epidermis war ebenfalls verringert. Es konnte gezeigt werden, dass die Effekte nicht von Schwankungen der ausgesäten Zellzahl ausgelöst wurden; auch war die Gesamtanzahl der

Zellen zwischen normaler und UV-RHE nicht auffällig anders. Dies läßt den Rückschluß zu, dass die verringerte Dicke durch abgeflachte und/oder die Abstoßung abgestorbener, verhornter Zellen zustande kam. Die Verdünnung stimmt überein mit der epidermalen Atrophie gealterter Haut, in der seneszente Zellen zu Struktur- und Funktionsveränderungen beitragen. Darüber hinaus wurde die Ausschüttung proinflammatorischer Zytokine (IL-1α, IL-6, IL-8, IL-12 und TNFα) getestet. Nur IL-1α und IL-8 waren oberhalb des Detektionslimits und über die gesamte Kulturdauer circa zweifach erhöht in 25 mJ/cm^2 UV-RHE gegenüber der normalen RHE. Der Spiegel an IL-1α war maximal erhöht nach zwei Tagen und ging den erhöhten Spiegeln von IL-8 zwischen Tag 7 und 14 voraus. Erhöhte Sekretion von IL-1α und IL-8 sind Teil des seneszenz-assoziierten sekretorischen Phenotyps (SASP), charakteristisch für die chronischen, niedrigschwellig entzündlichen Prozesse, die in alter Haut beobachtet wurden. Außerdem wurde in 25 mJ/cm^2 UV-RHE von wenigstens zwei Spendern erhöhte ß-Galaktosidaseexpression nachgewiesen. Zusammen mit den entsprechenden Ergebnissen aus dem Monolayer und der erhöhten IL-1α und -8 Sekretion sprechen die Ergebnisse für das Vorhandensein seneszenter Zellen in der UV-RHE, übereinstimmend mit dem Vorkommen seneszenter Zellen in gealterter Haut. Zur Untersuchung der Barrierefunktion wurde die Permeation von zwei OECD-Referenzsubstanzen getestet. Koffein und Testosteron permiierten durch UV-RHE schneller als durch die normale RHE. Trotz relativ starker spenderabhängiger Unterschiede wurde ein klarer Trend zur verringerten Barrierefunktion in 25 mJ/cm^2 UV-RHE festgestellt, in Übereinstimmung mit den strukturellen und funktionalen Veränderungen des Stratum corneums in gealterter Haut. Weiterhin wurde die Penetration von core-multishell- (CMS-) Nanocarriern getestet, die als innovative Transportsysteme für Wirkstoffe zur Behandlung von Hautkrankheiten entwickelt wurden. Obwohl bereits vielversprechende Ergebnisse vorliegen, ist ihre Risikobewertung noch nicht abgeschlossen; so wurden sie beispielsweise noch nicht auf der veränderten Barriere von gealterter Haut getestet. Passend zur verringerten Barriere der 25 mJ/cm^2 UV-RHE konnte eine gegenüber der normalen RHE zweifache (in das Stratum corneum) und sechsfache (in die viablen Schichten) erhöhte Penetration von mit Indocarbocyanin markierten Nanocarriern festgestellt werden (detektiert mittels FLIM, Fluorescence lifetime imaging microscopy). Insgesamt wurde eine neuartige rekonstruierte Epidermis aus UV-gestressten Keratinozyten aufgebaut, die die wichtigsten Kennzeichen *in vivo* gealterter Haut abbilden konnte. Die

Ähnlichkeit zeigte sich in der Morphologie, erhöhter IL-1α und IL-8 Sekretion, seneszenz-assoziierter ß-Galaktosidaseexpression sowie erhöhter Permeation und Penetration.

References

1. Farage, M.A., et al., *Intrinsic and extrinsic factors in skin ageing: a review.* Int J Cosmet Sci, 2008. **30**: p. 87-95.
2. Jiang, Z.X. and J. DeLaCruz, *Appearance benefits of skin moisturization.* Skin Res Technol, 2011. **17**: p. 51-55.
3. Lorencini, M., et al., *Active ingredients against human epidermal aging.* Ageing Res Rev, 2014. **15**: p. 100-115
4. White-Chu, E.F. and M. Reddy, *Dry skin in the elderly: complexities of a common problem.* Clin Dermatol, 2011. **29**: p. 37-42.
5. Kuwazuru, O., et al., *Skin wrinkling morphology changes suddenly in the early 30s.* Skin Res Technol, 2012. **18**: p. 495-503.
6. Bourguignon, L.Y., et al., *Selective matrix (hyaluronan) interaction with CD44 and RhoGTPase signaling promotes keratinocyte functions and overcomes age-related epidermal dysfunction.* J Dermatol Sci, 2013. **72**: p. 32-44.
7. Shlivko, I.L., et al., *Complex assessment of age-specific morphofunctional features of skin of different anatomic localizations.* Skin Res Technol, 2013. **19**: p. e85-92.
8. Cordisco, S., et al., *Bmi-1 reduction plays a key role in physiological and premature aging of primary human keratinocytes.* J Invest Dermatol, 2010. **130**: p. 1048-1062.
9. Elias, P.M. and R. Ghadially, *The aged epidermal permeability barrier: basis for functional abnormalities.* Clin Geriatr Med, 2002. **18**: p. 103-120, vii.
10. Cumberbatch, M., et al., *Epidermal Langerhans cell migration and sensitisation to chemical allergens.* APMIS, 2003. **111**: p. 797-804.
11. Ogden, S., et al., *The effect of ageing on phenotype and function of monocyte-derived Langerhans cells.* Br J Dermatol, 2011. **165**: p. 184-188.
12. Choi, E.H., et al., *Stratum corneum acidification is impaired in moderately aged human and murine skin.* J Invest Dermatol, 2007. **127**: p. 2847-2856.
13. Van Gele, M., et al., *Three-dimensional skin models as tools for transdermal drug delivery: challenges and limitations.* Expert Opin Drug Deliv, 2011. **8**: p. 705-720.
14. Schäfer-Korting, M., et al., *Reconstructed human epidermis for skin absorption testing: results of the German prevalidation study.* Altern Lab Anim, 2006. **34**: p. 283-294.
15. Kandarova, H., et al., *Assessment of the skin irritation potential of chemicals by using the SkinEthic reconstructed human epidermal model and the common skin irritation protocol*

evaluated in the ECVAM skin irritation validation study. Altern Lab Anim, 2006. **34**: p. 393-406.

16. Diekmann, J., et al., *A three-dimensional skin equivalent reflecting some aspects of in vivo aged skin.* Exp Dermatol, 2016. **25**: p. 56-61.
17. Pennacchi, P.C., et al., *Glycated reconstructed human skin as a platform to study the pathogenesis of skin aging.* Tissue Eng Part A, 2015. **21**: p. 2417-2425.
18. Dos Santos, M., et al., *In vitro 3-D model based on extending time of culture for studying chronological epidermis aging.* Matrix Biol, 2015. **47**: p. 85-97.
19. Lakatos, P., et al., *3-Aminobenzamide protects primary human keratinocytes from UV-induced cell death by a poly(ADP-ribosyl)ation independent mechanism.* Biochim Biophys Acta, 2013. **1833**: p. 743-751.
20. Rodier, F. and J. Campisi, *Four faces of cellular senescence.* J Cell Biol, 2011. **192**: p. 547-556.
21. Hayflick, L., *The limited in vitro lifetime of human diploid cell strains.* Exp Cell Res, 1965. **37**: p. 614-636.
22. Toussaint, O., et al., *Stress-induced premature senescence: from biomarkers to likeliness of in vivo occurrence.* Biogerontology, 2002. **3**: p. 13-17.
23. Greussing, R., et al., *Identification of microRNA-mRNA functional interactions in UVB-induced senescence of human diploid fibroblasts.* BMC Genomics, 2013. **14**: p. 224.
24. Coppe, J.P., et al., *The senescence-associated secretory phenotype: the dark side of tumor suppression.* Annu Rev Pathol, 2010. **5**: p. 99-118.
25. Campisi, J., *Cancer and ageing: rival demons?* Nat Rev Cancer, 2003. **3**(5): p. 339-349.
26. Williams, P.D. and T. Day, *Antagonistic pleiotropy, mortality source interactions, and the evolutionary theory of senescence.* Evolution, 2003. **57**: p. 1478-1488.
27. Kraemer, K.H., *Sunlight and skin cancer: another link revealed.* Proc Natl Acad Sci U S A, 1997. **94**: p. 11-14.
28. Lewis, D.A., et al., *The IGF-1/IGF-1R signaling axis in the skin: a new role for the dermis in aging-associated skin cancer.* Oncogene, 2010. **29**: p. 1475-1485.
29. Parrinello, S., et al., *Stromal-epithelial interactions in aging and cancer: senescent fibroblasts alter epithelial cell differentiation.* J Cell Sci, 2005. **118**: p. 485-496.
30. Harding, K.G., K. Moore, and T.J. Phillips, *Wound chronicity and fibroblast senescence--implications for treatment.* Int Wound J, 2005. **2**: p. 364-368.
31. Usui, M.L., et al., *Keratinocyte migration, proliferation, and differentiation in chronic ulcers from patients with diabetes and normal wounds.* J Histochem Cytochem, 2008. **56**: p. 687-696.

32. De Cecco, M., et al., *Nuclear protein accumulation in cellular senescence and organismal aging revealed with a novel single-cell resolution fluorescence microscopy assay.* Aging, 2011. **3**: p. 955-967.

33. Saretzki, G., *Cellular senescence in the development and treatment of cancer.* Curr Pharm Des, 2010. **16**: p. 79-100.

34. Deruy, E., et al., *MnSOD upregulation induces autophagic programmed cell death in senescent keratinocytes.* PLoS One, 2010. **5**: p. e12712.

35. Redon, C.E., et al., *Recent developments in the use of gamma-H2AX as a quantitative DNA double-strand break biomarker.* Aging, 2011. **3**: p. 168-174.

36. Galluzzi, L., et al., *Cell senescence: methods and protocols*. Methods Mol Biol, 2013. **965** in: L. Galluzzi et al (Ed.) Springer, doi 10.1007/978-1-62703-239-1_13

37. Freund, A., C.K. Patil, and J. Campisi, *p38MAPK is a novel DNA damage response-independent regulator of the senescence-associated secretory phenotype.* EMBO J, 2011. **30**: p. 1536-1548.

38. Itahana, K., G. Dimri, and J. Campisi, *Regulation of cellular senescence by p53.* Eur J Biochem, 2001. **268**: p. 2784-2791.

39. Lewis, D.A., et al., *UVB-induced senescence in human keratinocytes requires a functional insulin-like growth factor-1 receptor and p53.* Mol Biol Cell, 2008. **19**: p. 1346-1353.

40. Becker, T., and Haferkamp, S., *Senescence and senescence-related disorders,* in: Molecular mechanisms of cellular senescence. InTech, 2013. p. 25-50 http://dx.doi.org/10.5772/54120

41. Demidenko, Z.N., et al., *Paradoxical suppression of cellular senescence by p53.* Proc Natl Acad Sci U S A, 2010. **107**: p. 9660-9664.

42. Dimri, G.P., et al., *A biomarker that identifies senescent human cells in culture and in aging skin in vivo.* Proc Natl Acad Sci U S A, 1995. **92**: p. 9363-9367.

43. Itahana, K., J. Campisi, and G.P. Dimri, *Methods to detect biomarkers of cellular senescence: the senescence-associated beta-galactosidase assay.* Methods Mol Biol, 2007. **371**: p. 21-31.

44. Kurz, D.J., et al., *Senescence-associated (beta)-galactosidase reflects an increase in lysosomal mass during replicative ageing of human endothelial cells.* J Cell Sci, 2000. **113**: p. 3613-3622.

45. Debacq-Chainiaux, F., et al., *Protocols to detect senescence-associated beta-galactosidase (SA-betagal) activity, a biomarker of senescent cells in culture and in vivo.* Nat Protoc, 2009. **4**: p. 1798-1806.

46. Qin, J.Z., et al., *Regulation of apoptosis by p53 in UV-irradiated human epidermis, psoriatic plaques and senescent keratinocytes.* Oncogene, 2002. **21**: p. 2991-3002.

47. Kurdykowski, S., et al., *Ultraviolet-B irradiation induces differential regulations of hyaluronidase expression and activity in normal human keratinocytes.* J Photochem Photobiol B, 2011. **87**: p. 1105-1112.

48. Yuki, T., et al., *Characterization of tight junctions and their disruption by UVB in human epidermis and cultured keratinocytes.* J Invest Dermatol, 2011. **131**: p. 744-752.
49. Brandner, J.M., et al., *Epidermal tight junctions in health and disease.* Tissue Barriers, 2015. **3**: p. e974451.
50. Ruzsnavszky, O., et al., *UV-B induced alteration in purinergic receptors and signaling on HaCaT keratinocytes.* J Photochem Photobiol B, 2011. **105**: p. 113-118.
51. Wunderlich, L., et al., *UVB induces a biphasic response of HIF-1alpha in cultured human keratinocytes.* Exp Dermatol, 2008. **17**: p. 335-342.
52. Balogh, A., et al., *Reference genes for quantitative real time PCR in UVB irradiated keratinocytes.* J Photochem Photobiol B, 2008. **93**: p. 133-139.
53. Ghadially, R., et al., *The aged epidermal permeability barrier. Structural, functional, and lipid biochemical abnormalities in humans and a senescent murine model.* J Clin Invest, 1995. **95**: p. 2281-2290.
54. Prausnitz, M.R., S. Mitragotri, and R. Langer, *Current status and future potential of transdermal drug delivery.* Nat Rev Drug Discov, 2004. **3**: p. 115-124.
55. Korting, H.C. and Schäfer-Korting, M., *Carriers in the topical treatment of skin disease*. in: M. Schäfer-Korting (Ed.), Handb Exp Pharmacol, Springer, Heidelberg, 2010 p. 435-468.
56. Choksi, A.N., T. Poonawalla, and M.G. Wilkerson, *Nanoparticles: a closer look at their dermal effects.* J Drugs Dermatol, 2010. **9**: p. 475-481.
57. Schneider, M., et al., *Nanoparticles and their interactions with the dermal barrier.* Dermatoendocrinol, 2009. **1**: p. 197-206.
58. Küchler, S., et al., *Nanoparticles for skin penetration enhancement--a comparison of a dendritic core-multishell-nanotransporter and solid lipid nanoparticles.* Eur J Pharm Biopharm, 2009. **71**: p. 243-250.
59. Eckl, K.M., et al., *Increased cutaneous absorption reflects impaired barrier function of reconstructed skin models mimicking keratinisation disorders.* Exp Dermatol, 2014. **23**: p. 286-288.
60. Haag, S.F., et al., *Skin penetration enhancement of core-multishell nanotransporters and invasomes measured by electron paramagnetic resonance spectroscopy.* Int J Pharm, 2011. **416**: p. 223-228.
61. Küchler, S., et al., *Influence of nanocarrier type and size on skin delivery of hydrophilic agents.* Int J Pharm, 2009. **377**: p. 169-172.
62. Boreham, A., et al., *Nanodynamics of dendritic core-multishell nanocarriers.* Langmuir, 2014. **30**: p. 1686-1695.

63. Zoschke, C., et al., *Dendritic nanoparticles for cutaneous drug delivery--testing in human skin and reconstructed human skin.* Curr Pharm Des, 2015. **21**: p. 2784-2800.

64. Alnasif, N., et al., *Penetration of normal, damaged and diseased skin - An in vitro study on dendritic core-multishell nanotransporters.* J Control Release, 2014. **185**: p. 45-50.

65. Obrigkeit, D.H., et al., *Effects of photodynamic therapy evaluated in a novel three-dimensional squamous cell carcinoma organ construct of the skin.* J Photochem Photobiol B, 2009. **85**: p. 272-278.

66. Richter, C., et al., *Dual-fluorescence pH probe for bio-labelling.* Phys Chem Chem Phys, 2015. **17**: p. 30590-30597.

67. Boreham, A., et al., *Detecting and quantifying biomolecular interactions of a dendritic polyglycerol sulfate nanoparticle using Fluorescence Lifetime measurements.* Molecules, 2015. **21**: p. e22.

68. Crisan, D., et al., *Ultrasonographic assessment of skin structure according to age.* Indian J Dermatol Venereol Leprol, 2012. **78**: p. 519.

69. Frankart, A., et al., *Epidermal morphogenesis during progressive in vitro 3D reconstruction at the air-liquid interface.* Exp Dermatol, 2012. **21**: p. 871-875.

70. Honzke, S., et al., *Influence of Th2 cytokines on the cornified envelope, tight junction proteins, and ?-defensins in filaggrin-deficient skin equivalents.* J Invest Dermatol, 2016. **136**: p. 631-639.

71. Lewis, D.A., et al., *Reversing the aging stromal phenotype prevents carcinoma initiation.* Aging, 2011. **3**: p. 407-416.

72. Michaloglou, C., et al., *BRAFE600-associated senescence-like cell cycle arrest of human naevi.* Nature, 2005. **436**: p. 720-724.

73. Soroka, Y., et al., *Aged keratinocyte phenotyping: morphology, biochemical markers and effects of Dead Sea minerals.* Exp Gerontol, 2008. **43**: p. 947-957.

74. Perera, R.J., et al., *Defining the transcriptome of accelerated and replicatively senescent keratinocytes reveals links to differentiation, interferon signaling, and Notch related pathways.* J Cell Biochem, 2006. **98**: p. 394-408.

75. Wang, Y., et al., *Induced p53 expression in lung cancer cell line promotes cell senescence and differentially modifies the cytotoxicity of anti-cancer drugs.* Oncogene, 1998. **17**: p. 1923-1930.

76. Vigneron, A. and K.H. Vousden, *p53, ROS and senescence in the control of aging.* Aging, 2010. **2**: p. 471-474.

77. Bernard, D., et al., *Involvement of Rel/nuclear factor-kappaB transcription factors in keratinocyte senescence.* Cancer Res, 2004. **64**: p. 472-481.

78. Kosmadaki, M.G., et al., *UV induces VEGF through a TNF-alpha independent pathway.* FASEB J, 2003. **17**: p. 446-448.

79. Meloni, M., A. Farina, and B. de Servi, *Molecular modifications of dermal and epidermal biomarkers following UVA exposures on reconstructed full-thickness human skin.* Photochem Photobiol Sci, 2010. **9**: p. 439-447.

80. Romanov, V.S., et al., *p21(Waf1) is required for cellular senescence but not for cell cycle arrest induced by the HDAC inhibitor sodium butyrate.* Cell Cycle, 2010. **9**: p. 3945-3955.

81. Abramova, M.V., et al., *G1/S arrest induced by histone deacetylase inhibitor sodium butyrate in E1A + Ras-transformed cells is mediated through down-regulation of E2F activity and stabilization of beta-catenin.* J Biol Chem, 2006. **281**: p. 21040-21051.

82. OECD 428, *Test No. 428: skin absorption: in vitro method, in: OECD guidelines for the testing of chemicals, section 4: health effects*, available from: http://dx.doi.org/10.1787/9789264071087-en, 2004.

83. Lee, J.H., et al., *Acute effects of UVB radiation on the proliferation and differentiation of keratinocytes.* Photodermatol Photoimmunol Photomed, 2002. **18**: p. 253-261.

84. Bertrand-Vallery, V., et al., *Repeated exposures to UVB induce differentiation rather than senescence of human keratinocytes lacking p16(INK-4A).* Biogerontology, 2010. **11**: p. 167-181.

85. Tsugita, T., et al., *Positional differences and aging changes in Japanese woman epidermal thickness and corneous thickness determined by OCT (optical coherence tomography).* Skin Res Technol, 2013. **19**: p. 242-250.

86. Gilchrest, B.A., *Using DNA damage responses to prevent and treat skin cancers.* J Dermatol, 2004. **31**: p. 862-877.

87. Takeuchi, H. and T.M. Runger, *Longwave UV light induces the aging-associated progerin.* J Invest Dermatol, 2013. **133**: p. 1857-1862.

88. Kang, E.S., et al., *Aldose reductase in keratinocytes attenuates cellular apoptosis and senescence induced by UV radiation.* Free Radic Biol Med, 2010. **50**: p. 680-688.

89. Hayflick, L., *New approaches to old age.* Nature, 2000. **403**: p. 365.

90. Hayflick, L., *Aging and the genome.* Science, 1999. **283**: p. 2019.

91. Zoller, N.N., et al., *Evaluation of beneficial and adverse effects of glucocorticoids on a newly developed full-thickness skin model.* Toxicol In Vitro, 2008. **22**: p. 747-759.

92. Coppe, J.P., et al., *A human-like senescence-associated secretory phenotype is conserved in mouse cells dependent on physiological oxygen.* PLoS One, 2010. **5**: p. e9188.

93. Chaturvedi, V., et al., *Resistance to UV-induced apoptosis in human keratinocytes during accelerated senescence is associated with functional inactivation of p53.* J Cell Physiol, 2004. **198**: p. 100-109.

94. Wu, Y.Y. and J.L. Rees, *Variation in epidermal housekeeping gene expression in different pathological states.* Acta Derm Venereol, 2000. **80**: p. 2-3.

95. Di Micco, R., et al., *Interplay between oncogene-induced DNA damage response and heterochromatin in senescence and cancer.* Nat Cell Biol, 2011. **13**: p. 292-302.

96. Kosar, M., et al., *Senescence-associated heterochromatin foci are dispensable for cellular senescence, occur in a cell type- and insult-dependent manner and follow expression of p16(ink4a).* Cell Cycle, 2011. **10**: p. 457-468.

97. Janson, D., et al., *Effects of serially passaged fibroblasts on dermal and epidermal morphogenesis in human skin equivalents.* Biogerontology, 2013. **14**: p. 131-140.

98. Schäfer-Korting, M., et al., *The use of reconstructed human epidermis for skin absorption testing: Results of the validation study.* Altern Lab Anim, 2008. **36**: p. 161-187.

99. Netzlaff, F., et al., *Permeability of the reconstructed human epidermis model Episkin in comparison to various human skin preparations.* Eur J Pharm Biopharm, 2007. **66**: p. 127-134.

100. Waller, J.M. and H.I. Maibach, *Age and skin structure and function, a quantitative approach (I): blood flow, pH, thickness, and ultrasound echogenicity.* Skin Res Technol, 2005. **11**: p. 221-235.

101. Roskos, K.V., H.I. Maibach, and R.H. Guy, *The effect of aging on percutaneous absorption in man.* J Pharmacokinet Biopharm, 1989. **17**: p. 617-630.

102. Hachiya, A., et al., *Mechanistic effects of long-term ultraviolet B irradiation induce epidermal and dermal changes in human skin xenografts.* Am J Pathol, 2009. **174**: p. 401-413.

103. Duval, C., et al., *Key regulatory role of dermal fibroblasts in pigmentation as demonstrated using a reconstructed skin model: impact of photo-aging.* PLoS One, 2014. **9**: p. e114182.

104. Akase, T., et al., *Aging-like skin changes induced by ultraviolet irradiation in an animal model of metabolic syndrome.* Biol Res Nurs, 2012. **14**: p. 180-187.

105. Bernerd, F. and D. Asselineau, *An organotypic model of skin to study photodamage and photoprotection in vitro.* J Am Acad Dermatol, 2008. **58**: p. 155-159.

106. Regina, C., et al., *Vascular ageing and endothelial cell senescence: Molecular mechanisms of physiology and diseases.* Mech Ageing Dev, 2016.doi: 10.1016/j.mad.2016.05.003 (in press)

Abbreviations

ab – Antibody

ABU – Arbitrary brightness units

APS – Ammonium persulfate

BCA – Bicinchoninic acid

BrdU – 5-Bromo-2'-deoxyuridine

BPE – Bovine pituitary extract

BSA – Bovine serum albumin

cDNA – Complementary DNA

Ctrl – Control

DAPI – 4',6-Diamidine-2-phenylindol

ddH_2O – Double-distilled water

DEPC – Diethylpyrocarbonate

DNAse – Deoxyribonuclease

dNTP – Deoxynucleotide

DTT – Dithiothreitol

cp – Crossing points

cpm – Counts per minute

cyclin D – Cyclin-dependent kinase D

Da – Dalton

DAPI – 4', 6-Diamidino-2-phenylindole

DEPC – Diethylpyrocarbonate

DnTPs – Deoxynucleotides

DMEM – Dulbecco's modified Eagle's medium

DMSO – Dimethylsulfoxide

ECL – Enhanced chemiluminescence

ECM – Extracellular matrix

EDTA – Disodium ethylene-diamine tetraacetic acid

ELISA – Enzyme-linked immunosorbent assay

FCS – Fetal calve serum

GAPDH – Glyceraldehyde-3-phosphate dehydrogenase

GM-CSF – Granulocyte macrophage colony-stimulating factor

HE – Hematoxylin & Eosin staining

hEGF – Human epidermal growth factor

HGF – Hepatocyte growth factor

HRP – Horse raddish peroxidase

ICC – Indocarbocyanine

IL – Interleukin

KC – Keratinocytes

KGM – Keratinocyte growth medium

MMP – Matrix-metalloproteinase

MTT – 3-(4,5-Dimethylthiazol-2-yl)-2,5-diphenyltetrazolium bromide

mRNA – Messenger RNA

mTOR – Mammalian target of rapamycin

MTT – 3-(4,5-dimethyltiazol-2-yl)-2,5-diphenyltetrazolium bromide

NFkB – Nuclear factor kB

NHK – Normal human keratinocytes

NR – Nile red

OD – Optical density

OECD – Organisation for Economic Co-operation and Development

P_{app} – Permeation coefficient

PBS – Phosphate-buffered saline

PVDF – Polyvinylidene fluoride

$p16^{INK4a}$ – Cycline-dependent kinase inhibitor 2A

$p21^{WAF1}$ – Cycline-dependent kinase inhibitor 1

p38 MAP kinase – Mitogen-activated protein kinase 38

p53 – Tumor suppressor protein 53

Rbp – Recombination signal binding protein

RHE – Reconstructed human epidermis

RHS – Reconstructed human skin

RIPA buffer – Radio-Immunoprecipitation Assay buffer

RNAse – Ribonuclease

ROS – Reactive oxygen species

rpm – Rounds per minute

RT – Room temperature

RT-qPCR – Real-time quantitative polymerase chain reaction

SA-ß-gal – Senescence-associated ß-galactosidase

SAHF – Senescence-associated heterochromatin foci

SASP – Senescence-associated secretory phenotype

SC – Stratum corneum

SDS – Sodium dodecyl sulfate

SEM – Standard error of the mean

TBS – Tris-buffered saline

TBST – Tris-buffered saline with Tween 20

TEMED – Tetramethylethylenediamine

TJ – Tight-junction

TMB – Tetramethylbenzidine

TNFα – Tumor necrosis factor α

Tris – Tris(hydroxymethyl)aminomethane

UV – Ultraviolet

VE – Viable epidermis

VEGF – Vascular endothelial growth factor